Chapter 4

Fabrication of Ordered and High-Performance Nanostructured Photoelectrocatalysts by Electrochemical Anodization: Influence of Hydrodynamic Conditions

Bianca Lucas-Granados, Rita Sánchez-Tovar, Ramón M. Fernández-Domene and José García-Antón

Additional information is available at the end of the chapter

http://dx.doi.org/10.5772/intechopen.78303

Abstract

Nanostructured semiconductor metal oxides, such as TiO_2, WO_3, Fe_2O_3 or ZnO, are being widely investigated for their use as photoanodes, due to their higher surface areas in contact with the electrolyte, which increases the efficiency of photoelectrochemical processes. Metal oxide nanostructures have been synthesized by a number of different techniques. Anodization is one of the simpler methods used to synthesize nanostructured photoanodes, and the morphology and size of nanostructures can be designed by adequately controlling anodization parameters. Besides, these nanostructures are directly bound to the metallic back contact, improving significantly the efficiency of electron collection. It has been observed that hydrodynamic conditions during anodization (using a rotating disk electrode, RDE) greatly influenced the morphology of nanostructures and, therefore, their photoelectrochemical performance. The objective of this chapter is to review the innovative nanostructures with high-aspect ratios that can be fabricated by anodization under different hydrodynamic conditions.

Keywords: anodization, hydrodynamic conditions, nanostructure, photoelectrocatalysis, semiconductor

1. Introduction

Photoelectrochemistry (PEC) is a multidisciplinary area, which involves electrochemistry, materials science, solid-state physics and optics [1], and studies, in general, processes taking

place at the interface between an electrode and an electrolyte, under the influence of an illumination source. The most interesting part of PEC is related to the absorption of incident light in a semiconductor valence band. If the incident light energy is high enough (higher than the band-gap of the semiconductor, $h\upsilon \geq E_g$), this process results in electron excitation from the valence band to the conduction band, hence generating photogenerated electron/hole pairs (e^-/h^+). PEC has numerous attractive applications, such as the split of a water molecule in its fundamental constituents (gaseous hydrogen and oxygen), or the removal of persistent organic pollutants in water treatment processes. The schematic representation of PEC is depicted in **Figure 1**.

In that scheme, a common PEC cell with an n-type semiconductor photoanode and a metallic cathode (typically Pt) is presented. Upon illumination, electrons are promoted from the valence band to the conduction band and are subsequently driven toward the metallic back contact through the semiconductor bulk and, from there, to the cathode through the external circuit. Once in the cathode, these electrons can be used to reduce the oxidized redox species present in the electrolyte, such as water to form gaseous hydrogen. Photogenerated holes, which remain in the semiconductor valence band, are transported toward the semiconductor/electrolyte interface, where they can oxidize the reduced redox species present in the electrolyte, such as water to form gaseous oxygen or oxygen compounds, for example, hydroxyl radical, which could, in turn, directly oxidize recalcitrant organic pollutants (R in **Figure 1**) present in the aqueous solution. The movement of photogenerated charge carriers (e^-/h^+ pairs) described above takes place due to the development of a depleted space-charge region inside

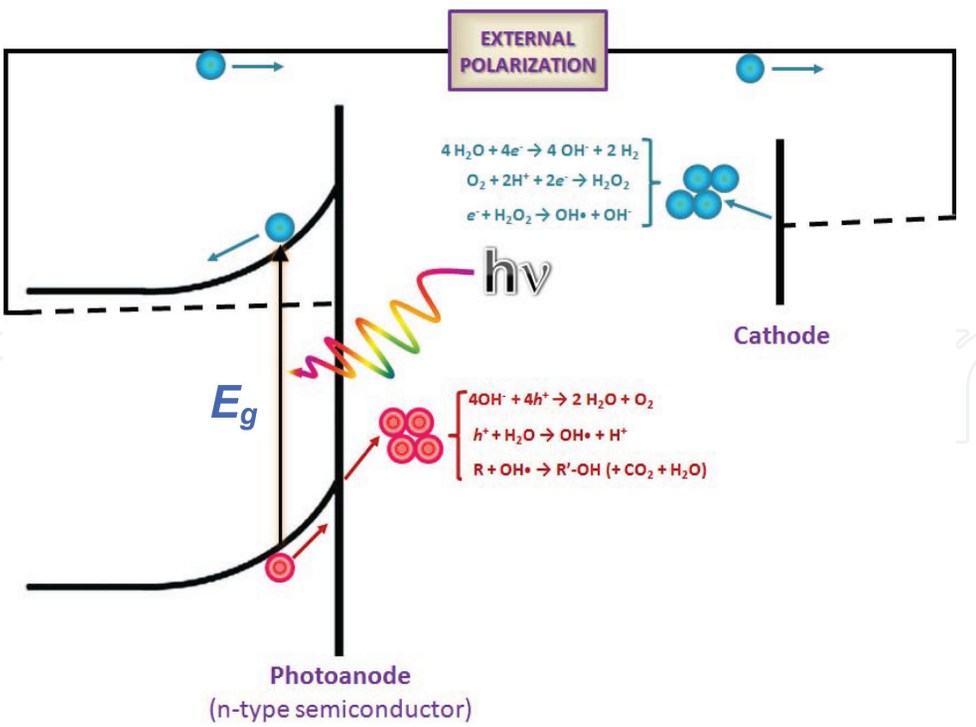

Figure 1. Schematic representation of a photoelectrochemical process.

the semiconductor, where the electric field acts on these charge carriers. To increase the thickness of this space-charge region and to sustain the electric field built up within it, a small external polarization is used in PEC. This polarization significantly improves the transport of electrons from the semiconductor conduction band to the cathode, hence increasing the lifetime of photogenerated charge carriers, minimizing the recombination of these carriers and, therefore, enhancing the PEC process overall efficiency [2–4].

The semiconducting photoanode is the central part of a PEC cell. Consequently, it is essential to develop strategies to fabricate efficient photoanodes, which is a materials science issue. Hence, the development of PEC is closely related to the advances achieved in the design and synthesis of materials used as photoanodes, in which the understanding of their properties and characteristics is fundamental. Among the most important characteristics, an efficient photoanode must satisfy the following [1, 5, 6]:

- **Appropriate bandgap energy (E_g)**. The bandgap is the smallest energy difference between the lowest edge of the conduction band and the highest edge of the valence band. A photoanode material should have bandgap energy high enough as to assure that the desired electrochemical reactions can take place (e.g., ~2 eV for water splitting, taking into account electrochemical losses and kinetic aspects [5], but not so high as to severely reduce the amount of usable solar radiation.

- **Appropriate band edge positions.** For hydrogen evolution, the conduction band edge must be positioned above hydrogen evolution, that is, at a more negative potential than that of the normal hydrogen electrode (NHE). For oxygen evolution, the valence band edge must be positioned below the oxygen evolution, that s, at a potential more positive than 1.23 V versus NHE. For generation of hydroxyl radicals, the position of the valence band edge must be located at potentials as high as 2.02 V versus NHE [7].

- **Suitable flat-band potential (E_{FB}).** The flat-band potential is the potential that needs to be applied to the semiconductor to reduce the band bending to zero, that is, at this potential, there is no depleted space charge layer and, therefore, no electric field inside the photoanode. The flat-band potential affects the recombination probability of photogenerated charge carriers: in general, the more negative the value of E_{FB}, the higher the potential drop at the depletion space charge layer and, consequently, the stronger the electrical field within the depleted space charge layer, which is the driving force to separate the photogenerated electron-hole pairs [5, 6, 8].

- **Good electrical conductivity.** Once electrons have been promoted from the valence band to the conduction band of the semiconductor photoanode due to light irradiation, a fast charge separation is crucial for efficient photoelectrochemical processes. For this, the transport of electrons and holes in the material must be good. The electrical conductivity of the photoanode material can be modified by modifying its defect disorder. The density of defects inside the semiconductor (i.e. vacancies, interstitial elements, etc.) must be high enough to enhance electrical conductivity but not so high to negatively affect the efficiency by favoring the recombination of charge carriers.

- **Good chemical, electrochemical and photoelectrochemical stability.** Photoanodes must be stable under prolonged exposure to the electrolyte under the operation conditions (applied potential and illumination).

In recent years, increasing attention is being paid to the design and synthesis of nanostructured metal oxides due to their exceptional properties. Photocurrent density obtained in PEC systems has two main contributions, one coming from the electrocatalytic process and other arising from the photon absorption process. The electrocatalytic process consumes the photogenerated charge carriers and it can become the rate-determining step of the PEC process (the charge transfer at the semiconductor/electrolyte interface) [4]. Current densities in electrochemistry are directly influenced by the real surface active area, since increasing surface area enhances the number of electroactive sites; therefore, nanostructuring the photoelectrode can improve its electrocatalytic performance. Moreover, in nanostructured photoelectrodes, the diffusion path of photogenerated holes toward the semiconductor/electrolyte interface is significantly shorter, which reduces electron-hole recombination. On the other hand, by roughening the semiconductor surface, direct light reflection is reduced due to the scattering of reflected photons, enhancing thus the chance of light absorption by the semiconductor and the possibility of further photoexcitation. Consequently, creating nanostructured photoanodes has immediate benefits on both their electrocatalytic activity and photoactivity [4].

During the last decades, several n-type semiconductor metal oxides, such as TiO_2, WO_3, Fe_2O_3 and ZnO, have been investigated as potential candidates for photoanode materials in PEC cells due to their different characteristics.

Titanium oxide (TiO_2) is a wide bandgap semiconductor ($E_g \approx 3.2$ eV in the anatase crystalline form [3, 4, 9], equivalent to a maximum wavelength of ~390 nm) with an exclusive set of properties, such as high chemical stability, resistance to photocorrosion and favorable band-edge position relative to the redox potentials for the decomposition of water, allowing the use of light for effective direct water splitting [5, 10, 11]. However, due to its high E_g, TiO_2 absorb photons only in the UV range, which represents a very small part of the solar spectrum.

Tungsten oxide (WO_3) is another attractive photoanode material owing to its high electron mobility and moderate hole diffusion length (≈150 nm). Besides, WO_3 can also absorb a part of the visible rays of the solar spectrum (its $E_g \approx 2.6$ eV, which corresponds approximately to a wavelength of $\lambda = 480$ nm) [3, 12, 13]. Moreover, in contrast with almost the rest of semiconductor oxides used as photoelectrocatalysts, WO_3 can safely operate in acidic environments, which is very useful in the treatment of low-pH wastewater [11].

Hematite (α-Fe_2O_3) is the most thermodynamically and stable iron oxide form under ambient conditions and it is a non-toxic, chemically stable and low cost material. Furthermore, it has a bandgap of $E_g \approx 2.1$ eV which indicates its suitability for visible light absorption up to ~590 nm, that is, hematite can collect up to ~40% of solar spectrum energy [4, 11]. Apart from its properties, hematite has some drawbacks such as low carrier mobility and short holes diffusion lengths, which can be overcome by nanostructuring the material.

Zinc oxide (ZnO) is also a wide bandgap semiconductor (E_g = 3.37 eV; λ = 369 nm) with similar characteristics as TiO_2 but with the advantage that ZnO possesses a higher electron mobility (from 10 to 100 times higher in comparison with TiO_2), that is, a large conductivity which makes ZnO a very suitable and promising substitute of TiO_2 [14, 15]. In spite of this, photogenerated electron-hole pairs tend to recombine fast in ZnO, so the use of hybrid semiconductors systems between ZnO and ZnS has been proposed to overcome this inconvenience [16, 17].

In order to prepare nanostructures of the oxides described above, various methodologies have been reported, such as sol-gel processes, hydrothermal and solvothermal methods, deposition processes or anodization. Of these, anodization is a fast and simple method to synthesize metal oxide nanostructures [12, 18–22]. With anodization, surface morphology can be designed by adequately controlling several parameters, such as the anodization potential, duration, electrolyte composition, temperature, and so on. Hence, the morphology and dimensions of nanostructures fabricated by anodization, as well as their PEC behavior, can be controlled by adjusting the aforementioned parameters. Moreover, nanostructures formed by anodization can be grown directly on the substrate (the back metal collector), thus avoiding compaction or sintering of nanostructures. This fact significantly reduces the contact resistance between the nanostructure and the metallic substrate, providing the basis for efficient charge collection. Therefore, anodization offers a robust and economical way to fabricate nanostructured metallic oxides.

Among the parameters that can be controlled to design and fabricate high-performance oxide nanostructures by anodization, hydrodynamic conditions during the synthesis process can be of great importance. Indeed, depending on the used material and the operation conditions, the mechanisms of nanostructures formation by anodization may involve one or more stages where mass transfer becomes the rate-determining step [8, 23]. Therefore, hydrodynamic

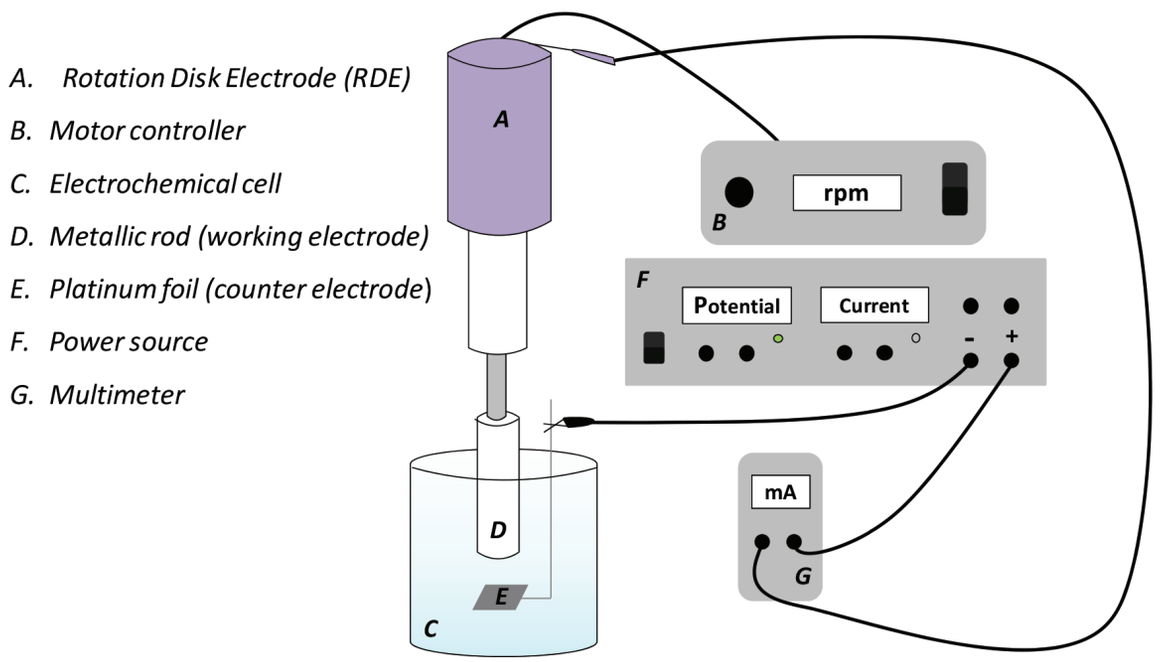

Figure 2. Experimental setup used during all the anodization processes, showing the electrode configuration.

conditions can play a central role in the synthesis of nanostructures by anodization. This chapter presents a review of the innovative high-performance nanostructures that have been fabricated by anodization under different hydrodynamic conditions. Although various fabrication conditions have been used, depending on the material, in all cases, hydrodynamic conditions have been controlled by connecting rods of the different metals to a rotating disk electrode (RDE) to assure reproducible mechanical convection of the electrolyte near the electrode surface. **Figure 2** shows an illustration of the electrode configuration used during all the anodization processes. The specific synthesis conditions for the different materials are detailed in the following sections.

2. TiO_2

Influence of hydrodynamic conditions for nanostructures formed from titanium (Ti) anodization is presented for samples synthesized in two different electrolytes and anodization conditions: ethylene glycol +1 M H_2O containing 0.05 M NH_4F and glycerol/water (60:40 vol.%) containing 0.27 M NH_4F. When anodization was performed in ethylene glycol based electrolytes 55 V for 30 min were directly applied to anodize the Ti. Nevertheless, in glycerol based electrolytes the potential was increased from 0 to 30 V at a rate of 200 mV s^{-1}, applying subsequently the potential of 30 V for 3 h. The active anode area exposed to the electrolyte was 0.5 cm^2.

2.1. Morphological characterization

Since the morphology of the nanostructures is highly dependent on the electrolyte used for anodization, the discussion of the influence of Reynolds number on the morphological properties of the TiO_2 nanostructures will be discussed for each particular anodization media. A field emission scanning electron microscope (FESEM) was used to characterize the morphology of the nanostructures.

Nanostructures anodized in ethylene glycol based electrolytes present an initiation layer which blocks the mouth of the nanotubes, preventing part of the solar radiation from being absorbed at the photoelectrode (**Figure 3a**). It was observed that rotating the electrode during anodization, part of the initiation layer was removed, and this elimination was more important as Reynolds number (Re) was increased (**Figure 3b**).

On the other hand, the hydrodynamic conditions completely changed the morphology of the formed nanostructures when anodization was carried out in glycerol based electrolytes, that is from nanotubes (at Re = 0, **Figure 4a**) to nanosponges (at Re > 0, **Figure 4b**). Nanosponge morphology is characterized by a connected and highly porous TiO_2 structure.

2.2. Anodization profile: current densities vs. time

The formation and growth of the TiO_2 nanostructures was monitored by recording the current density-time behavior (**Figure 3c** and **4c**). The current density profile follows a similar trend regardless the electrolyte used for anodization.

http://dx.doi.org/10.5772/intechopen.78303

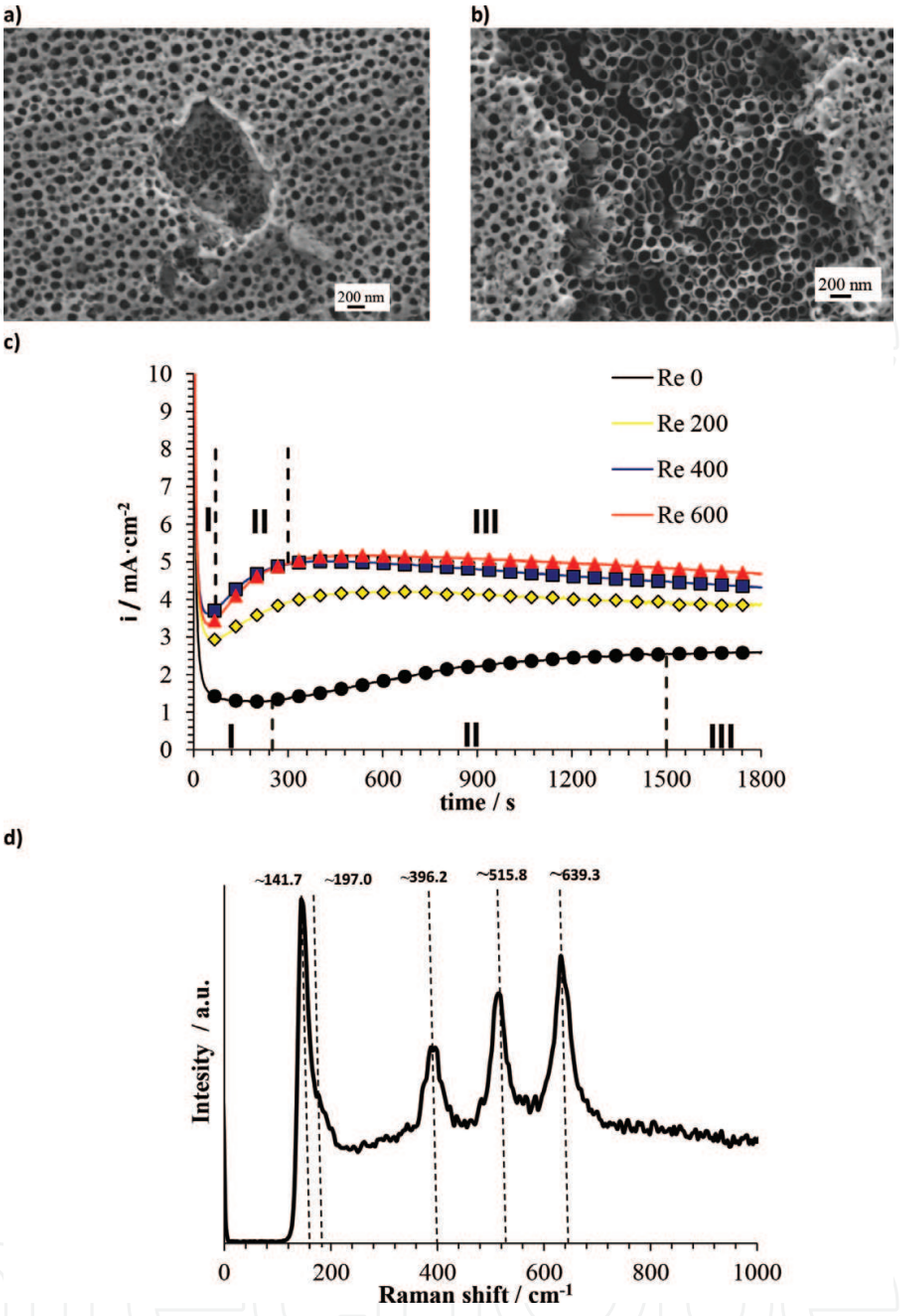

Figure 3. FESEM images of the nanostructures anodized in ethylene glycol-based electrolytes at a Re 600 (a and b). Current density versus time profiles of the nanostructures during anodization in ethylene glycol based electrolytes at the different hydrodynamic conditions (Re from 0 to 600) (c). Raman spectrum of a nanostructure anodized at re = 600 in ethylene glycol-based electrolytes and annealed in air at 450°C for 1 h (d).

In the first stage (I), current density decreases with time due to a compact TiO_2 oxide layer formation [9, 24]. Then, in the second stage (stage II), an increase in current density indicates the onset of TiO_2 dissolution due to the presence of fluoride ions in the electrolyte (stage II), according to the reaction shown in Eq. 1 [25–27].

$$TiO_2 + 6F^- + 4H^+ \rightarrow [TiF_6]^{2-} + 2H_2O \quad (1)$$

After that, in the third stage (stage III), current density remains almost constant due to the formation and growth of regular nanotubes or nanosponges [9, 28].

In general, **Figures 3c** and **4c** show that current densities increase with increasing Re in all the stages, which indicates that hydrodynamic conditions enhance the electrochemical processes taking place during anodization.

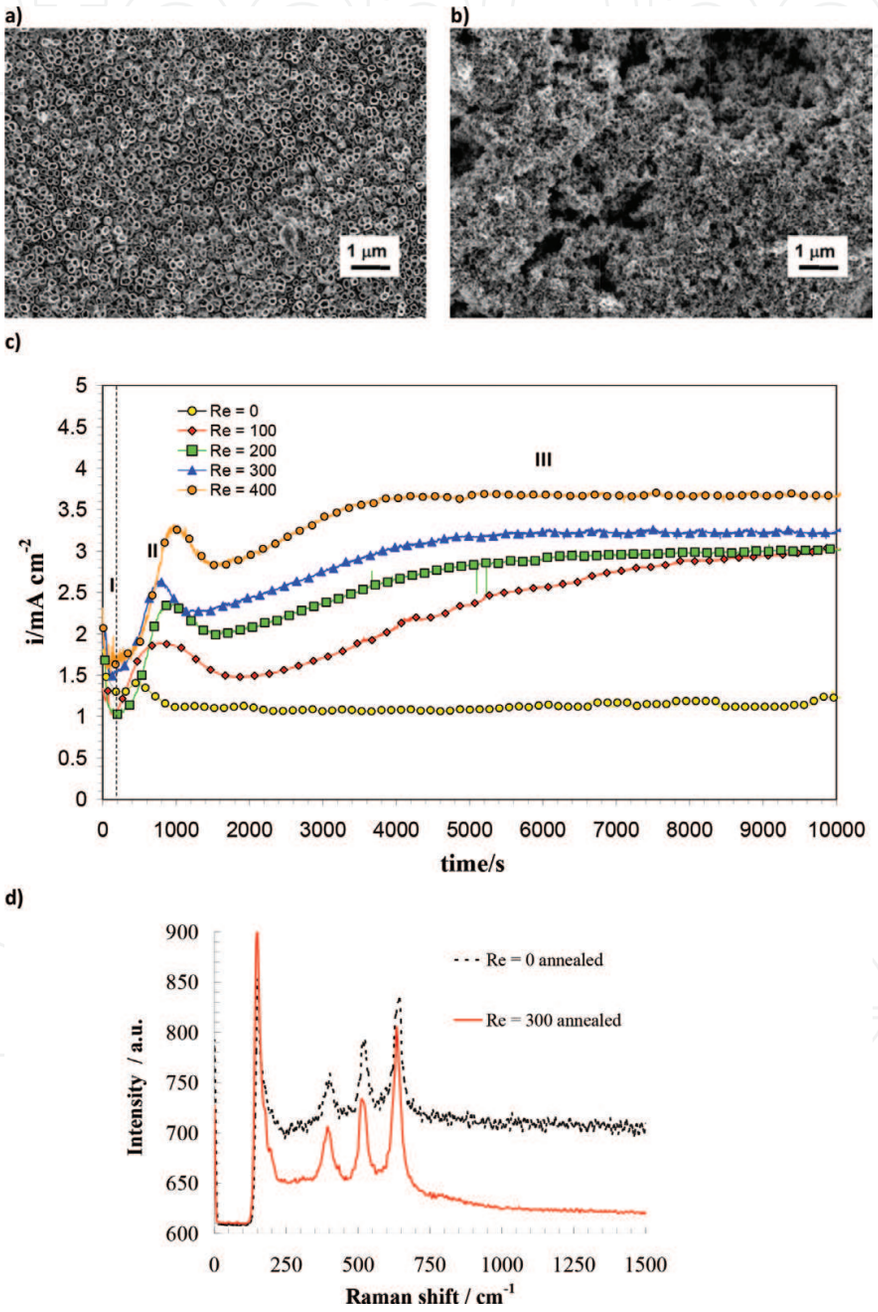

Figure 4. FESEM images of the nanostructures anodized in glycerol based electrolytes at a re = 0 (a) and re = 300 (b). Current density vs. time profiles of the nanostructures during anodization in ethylene glycol based electrolytes at the different hydrodynamic conditions (re from 0 to 400) (c). Raman spectra of the nanostructures anodized in glycerol based electrolytes, at re = 0 and re = 300 and annealed in air at 450°C for 1 h (d).

http://dx.doi.org/10.5772/intechopen.78303

2.3. Crystalline structure characterization

In order to obtain a crystalline structure, samples were annealed in air at 450°C for 1 h. After the annealing treatment, all the samples possessed the Raman peaks of the TiO_2 anatase phase shown in **Figures 3d** and **4d** (peaks at roughly 141.7, 197.0, 396.2, 515.1 and 639.3 cm^{-1} [28–30]).

2.4. Electrochemical and photoelectrochemical characterization

Electrochemical impedance spectroscopy (EIS) measurements at open circuit potential (OCP) and Mott-Schottky plots were performed in 0.1 M Na_2SO_4 in order to evaluate the electrochemical properties of the samples. **Figure 5** shows the Nyquist (**Figure 5a**), Bode-phase (**Figure 5b**) and Bode-modulus (**Figure 5c**) plots for the nanostructures anodized in ethylene glycol-based electrolytes.

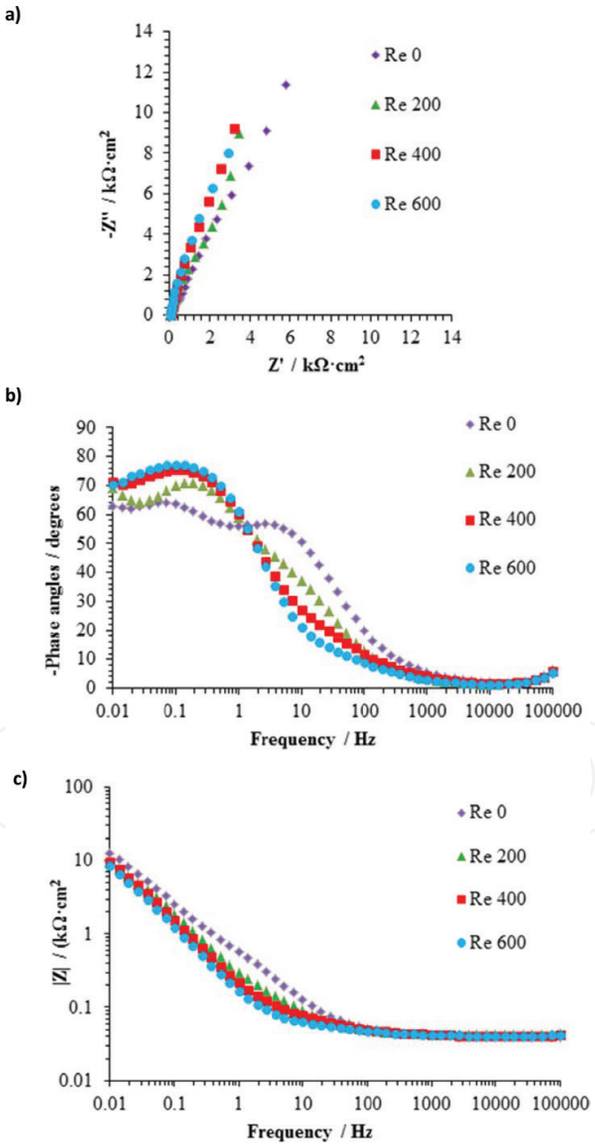

Figure 5. Experimental Nyquist (a), bode-phase (b) and bode-modulus (c) plots for the nanostructures anodized in ethylene glycol based electrolytes at Reynolds numbers = 0, 200, 400 and 600. Experiments performed in 0.1 M Na_2SO_4.

Figure 6 shows the electrical equivalent circuit used to fit EIS data, where R_s is the electrolyte resistance, and the two groups of resistances and constant phase elements (R-CPE) correspond to the nanotubular layer (R_1-CPE_1) and the compact TiO_2 underlayer (R_2-CPE_2) [8, 31, 32].

The different parameters obtained from the fitting of the EIS data in the electrical equivalent circuit are shown in **Table 1**. From **Table 1**, it is important to highlight that the resistance of the compact layer is always higher than the one obtained for the nanotubes ($R_2 > R_1$), due to the higher conductivity of the nanostructures. On the other hand, R_1 decreases as Reynolds number increases, that is, the conductivity of the nanotubes increases at higher hydrodynamic conditions.

In order to observe the electrochemical behavior of nanostructures formed in glycerol-based electrolytes, **Figure 7** shows the Mott-Schottky (MS) plots at a frequency of 10 kHz (to eliminate the capacitance dependence on frequency) for nanotubes (Re = 0) and nanosponges (Re > 0).

In **Figure 7**, positive slopes of the MS plots are characteristic of *n*-type semiconductors. The dominant TiO_2 defects are oxygen vacancies due to their lower formation energy compared with Ti^{3+} interstitials [32–38]. **Table 2** shows the donor densities (N_D) and the flat band potential (E_{FB}) values at different Re.

The donor density can be determined from the positive slopes of the straight lines in the MS plots using the Mott-Schottky equation for an *n*-type semiconductor:

$$\frac{1}{C^2} = \frac{2}{\varepsilon_r \varepsilon_0 e N_D}\left(E - E_{FB} - \frac{kT}{e}\right) \quad (2)$$

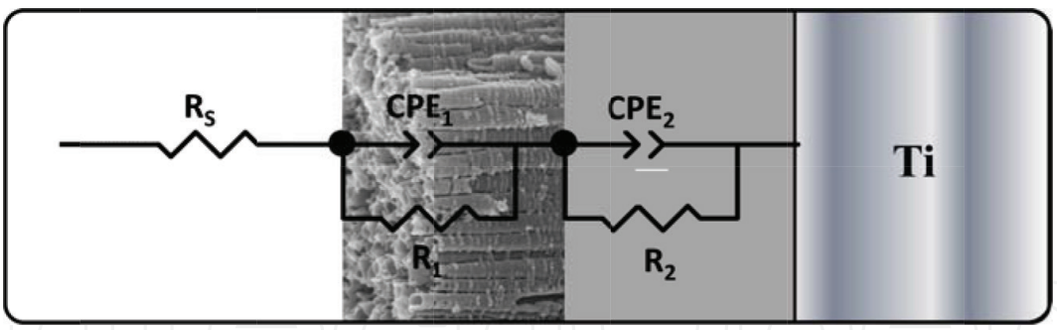

Figure 6. Electrical equivalent circuit used to simulate the experimental data obtained from EIS experiments shown in **Figure 5**.

Re	R_S/Ω cm^2	C_1/μF cm-2	α_1	R_1/kΩ cm2	C_2/μF cm^{-2}	α_2	R_2/kΩ cm^2	χ^2 (x10^{-3})
0	38 ± 4	106 ± 14	0.68 ± 0.03	5.7 ± 1.8	1690 ± 78	0.98 ± 0.02	78.3 ± 21	5.3
200	39 ± 3	279 ± 11	0.63 ± 0.04	5.1 ± 1.3	1903 ± 84	0.95 ± 0.01	39.4 ± 23	9.6
400	42 ± 5	475 ± 17	0.56 ± 0.08	4.4 ± 1.5	1942 ± 101	0.95 ± 0.03	24.8 ± 12	8.5
600	34 ± 7	132 ± 18	0.74 ± 0.07	2.5 ± 1.0	2399 ± 97	0.97 ± 0.04	38.4 ± 11	8.0

Table 1. Experimental values obtained from the equivalent circuit fitting for the nanostructures anodized in ethylene glycol-based electrolytes at the different Re = 0, 200, 400 and 600.

http://dx.doi.org/10.5772/intechopen.78303

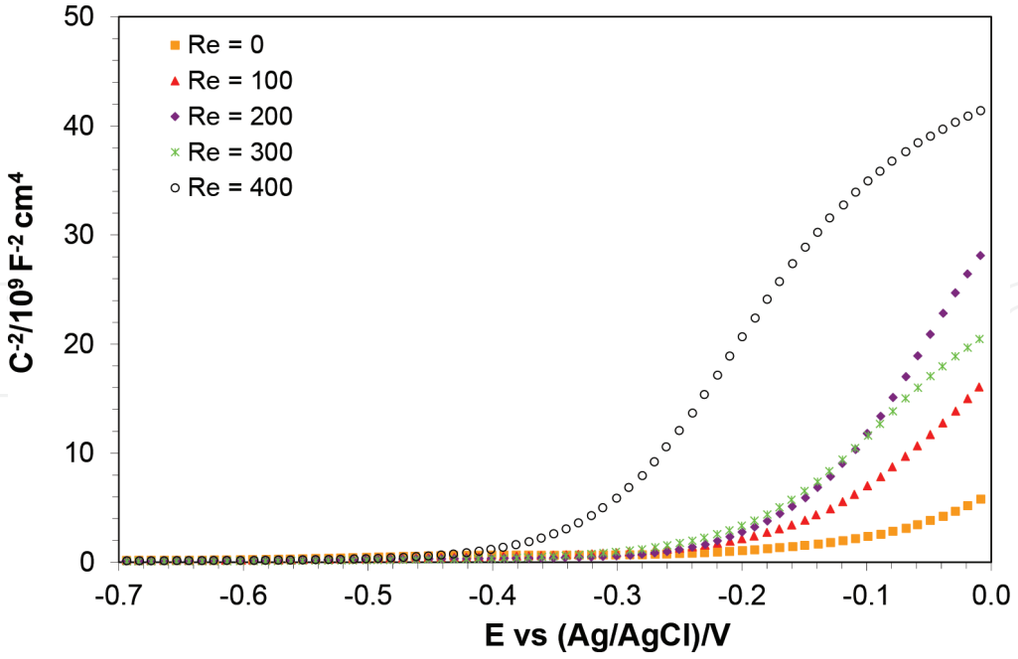

Figure 7. Mott-Schottky plots of the different nanostructures (nanotubes at Re = 0 and nanosponges at Re > 0) anodized in glycerol based electrolytes. Experiments performed in 0.1 M Na_2SO_4.

Re	N_D ($\times 10^{19}$ cm^{-3})	E_{FB}/V vs (Ag/AgCl)
0	3.6 ± 0.6	-0.15 ± 0.07
100	1.4 ± 0.3	-0.17 ± 0.04
200	1.1 ± 0.1	-0.17 ± 0.02
300	1.1 ± 0.2	-0.21 ± 0.01
400	0.9 ± 0.1	-0.33 ± 0.03

Table 2. Values of N_D and E_{FB} for the different nanostructures synthetized in glycerol-based electrolytes under static (Re = 0) and under hydrodynamic conditions (Re = 100, 200, 300 and 400).

where ε is the dielectric constant of the TiO_2 layers (100 for TiO_2 nanostructures [39]), ε_0 is the vacuum permittivity ($8.85 \cdot 10^{-14}$ F/cm), e is the electron charge ($1.60 \cdot 10^{-19}$ C) and σ is the positive slope of each straight line in the MS plots.

Table 2 shows that N_D decreases with increasing Re, that is, N_D is lower for the nanosponges than for the nanotubes. In this case, the increase in N_D leads to a decrease in the depletion layer thickness, resulting in an increase of recombination losses [6, 40, 41]. In fact, oxygen vacancies in TiO_2 act as recombination centers for electron and holes, playing a critical role in the trapping process [42–44].

Table 2 also shows the flat band potentials for the different nanostructures obtained in glycerol-based electrolytes. These values were determined from the intercept of the straight line in MS plots with the potential axis. To reduce the recombination probability, flat band potentials

should be high and negative [6, 42]. It can be observed in **Table 2** that flat band potentials are more negative with increasing Re, that is, nanosponges formed under hydrodynamic conditions possess more negative flat band potentials than nanotubes formed under static conditions. Thus, the charge recombination probability is lower in the case of the nanosponges.

Figure 8 shows the photoelectrochemical water splitting performance under simulated sunlight AM 1.5 conditions in 1 M KOH for the different nanostructures anodized in ethylene glycol (**Figure 8a**) and glycerol (**Figure 8b**)-based electrolytes.

It can be observed in terms of the photocurrent transient vs. potential curves that the nanostructures obtained under hydrodynamic conditions present a higher performance in comparison with the nanostructures anodized at the same potential, time and electrolyte but at

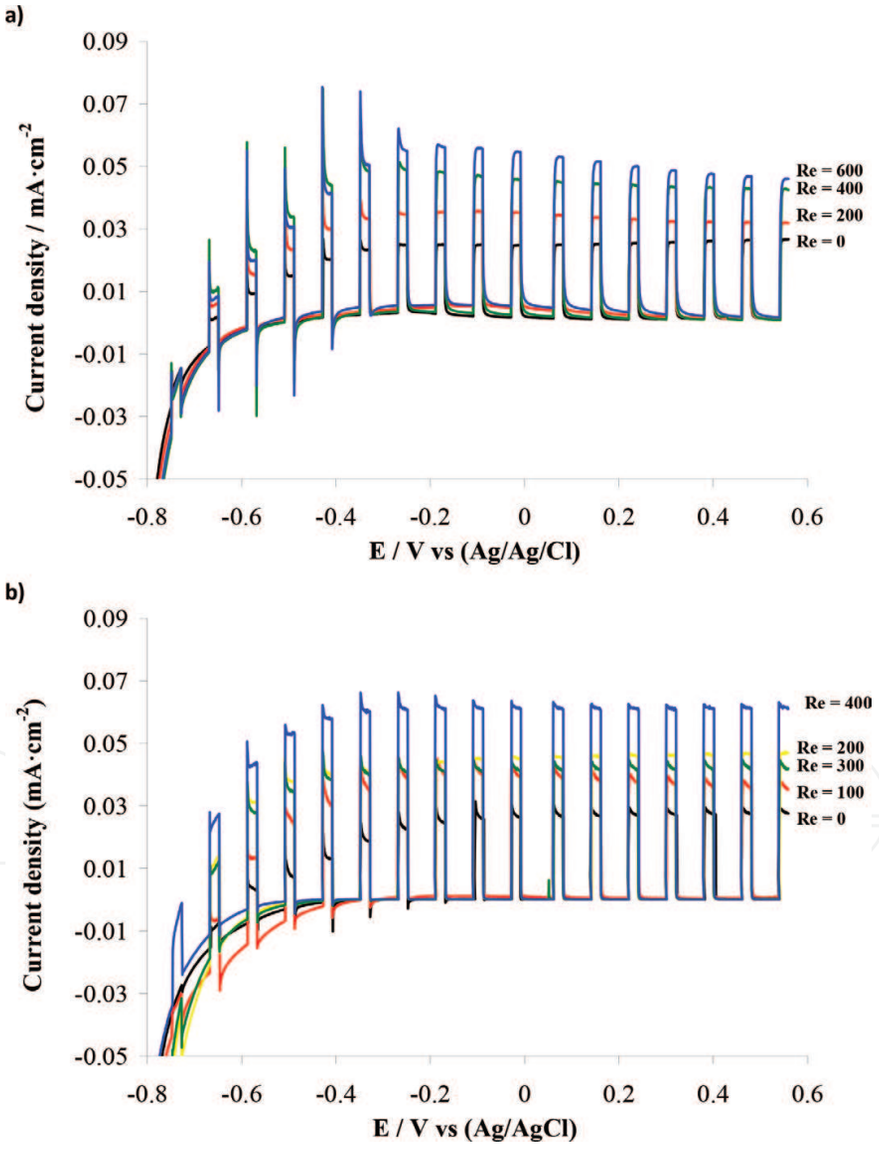

Figure 8. Current density versus applied potential profiles under dark and illumination conditions for the different nanostructures anodized under static (Re = 0) and at different hydrodynamic conditions (Re > 0) in ethylene glycol (a) and glycerol (b)-based electrolytes. Experiments were performed in 1 M KOH.

http://dx.doi.org/10.5772/intechopen.78303

Re = 0. These results are in agreement with the morphology of the samples (high surface area for the nanostructures anodized under hydrodynamic conditions), EIS measurements (low resistance values, i.e., high conductivity for nanostructures synthetized at Re > 0) and MS plots (appropriate donor density values and more negative flat band potentials).

Therefore, on the one hand, hydrodynamic conditions are beneficial in ethylene glycol-based electrolytes because of the removal of the initiation layer which offers a high surface area for photoelectrochemical water splitting. On the other hand, nanosponges formed in glycerol based electrolytes under dynamic conditions enhance the rate of the photoelectrochemical reaction over the photoelectrode due to their surface-active sites.

3. WO_3

Different WO_3 nanostructures synthesized by anodization have been presented in the literature in the past few years. Several morphologies have been obtained, such as nanopores [19, 45–52], nanoplatelets [53–55], nanoparticles [56], flower-shape nanostructures [57], and so on. Recently, we have presented novel WO_3 nanostructures fabricated by anodization under different controlled hydrodynamic conditions and, in general, photoresponses significantly higher than those for nanostructures synthesized under static conditions were obtained.

These nanostructures were produced by anodization of tungsten rods in sulfuric acid media in the presence of small amounts of complexing agents (NaF and H_2O_2). For example, tree-like globular clusters of WO_3 nanoplatelets were obtained in a 1.5 M H_2SO_4 + 0.1 M NaF electrolyte and at different rotation velocities of the RDE. **Figure 9** shows the FE-SEM images of the samples anodized in that electrolyte at different rotation velocities (0 and 375 rpm) [23, 58]. It can be observed that in both cases, the nanostructures formed on the tungsten surface presented nanoplatelet morphology, as other authors reported when anodizing in similar acid electrolytes [53–55, 57, 58]. Nevertheless, the morphology and dimensions of these nanoplatelets varied noticeably with rotation speed. At 0 rpm (**Figure 9a**), nanoplatelets grew quite orthogonal to the electrode surface, in a more or less ordered way. At 375 rpm (**Figure 9b**), nanoplatelets formed globular clusters that grew in a tree-like manner, forming a multilevel WO_3 layer resembling a forest seen from above. It is perceptible that the new nanostructure obtained under controlled hydrodynamic conditions exposed more surface area to the electrolyte than the one synthesized at 0 rpm.

In the presence of other well-known complexing agent of tungsten—hydrogen peroxide—and under controlled hydrodynamic conditions, a different nanostructure was obtained [59]. In this case, anodization of tungsten in a 1.5 M H_2SO_4 + 0.05 M H_2O_2 and at 375 rpm (the same rotation speed as in the example shown above for the NaF electrolyte), resulted in very small nanoplatelets or nanosheets forming a kind of spongy layer **(Figure 10**).

The three nanostructures shown in **Figures 9** and **10** shared a common formation mechanism, that is, a dissolution/precipitation mechanism, although it was greatly influenced by hydrodynamic conditions. In order to study the influence of rotation speed of the electrode on the

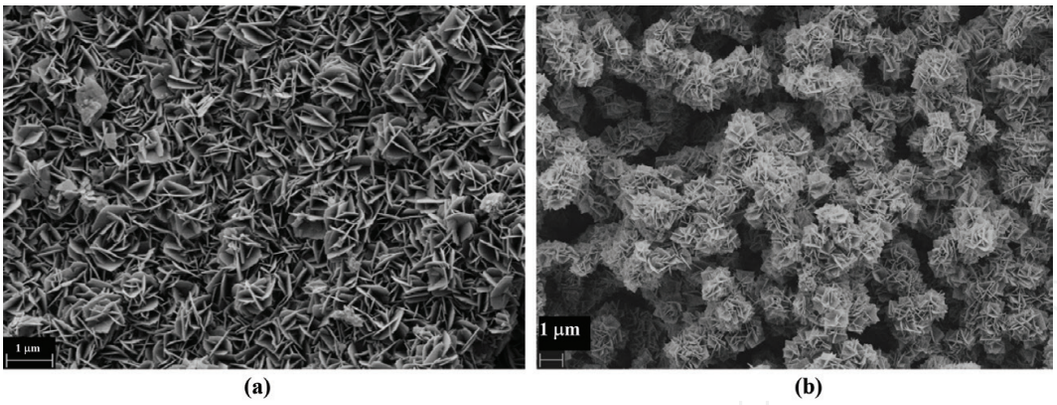

Figure 9. FE-SEM images of the samples anodized in the 1.5 M H_2SO_4 + 0.1 M NaF electrolyte at 0 rpm (a) and 375 rpm (b).

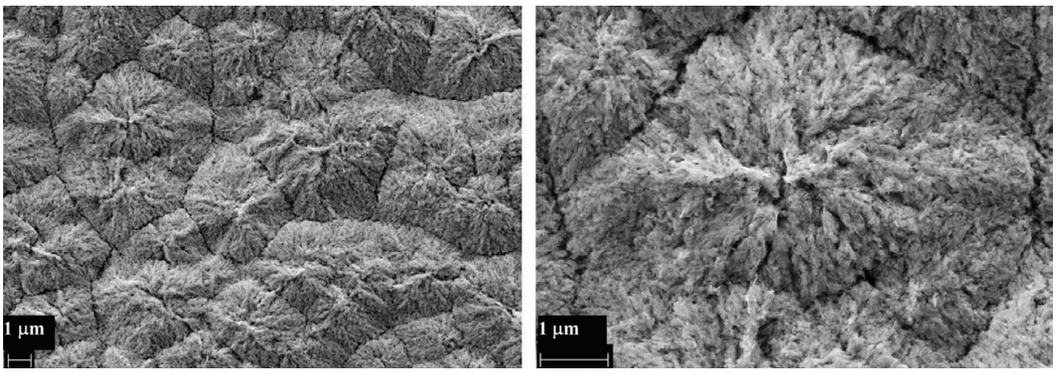

Figure 10. FE-SEM images of the samples anodized in the 1.5 M H_2SO_4 + 0.05 M H_2O_2 electrolyte at 375 rpm and at different magnifications.

formation and growth of WO_3 nanoplatelets, current density transients were recorded during the anodization processes. **Figure 11** shows, by way of illustration, current density transients recorded for the WO_3 nanostructures anodized in the 1.5 M H_2SO_4 + 0.1 M NaF electrolyte, under static (0 rpm) and hydrodynamic conditions (375 rpm).

During the first seconds of anodization, a notable decrease in current density can be observed for both cases. This decrease has been associated with the formation of a compact WO_3 layer on the electrode surface [19, 23, 58, 60]. Subsequently, current density started increasing, indicating the dissolution of the WO_3 layer due to the effect of H^+ and F^- [23, 58, 61]. This dissolution process resulted in the release of soluble cationic species, such as WO_2^{2+} (or $[W(OH)_4(H_2O)_4]^{2+}$ in its hydrated form) or $[WF_n]^{(6-n)}$, from the electrode surface. Afterward, current density gradually decreased again, eventually reaching a steady-state value. This decrease and the later stabilization of current density can be explained by the precipitation of soluble species upon reaching supersaturation conditions near the electrode surface. In fact, as the dissolution of the WO_3 layer proceeded, increasing amounts of tungsten cationic species were formed and they reacted to produce polycondensed tungstates [62]. These species finally precipitated on the electrode surface in the form of insoluble and highly polymeric tungstic acids ($WO_3 \bullet H_2O$ and $WO_3 \bullet 2H_2O$) due to strongly acidic pH of the electrolyte

http://dx.doi.org/10.5772/intechopen.78303

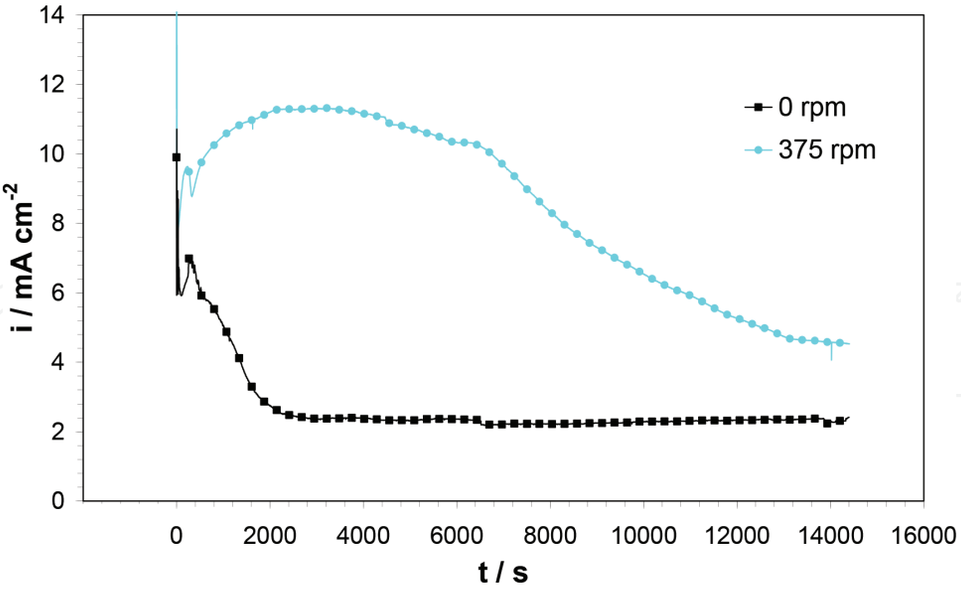

Figure 11. Current density transients recorded during anodization for the WO_3 nanostructures fabricated in the 1.5 M H_2SO_4 + 0.1 M NaF electrolyte, under static (0 rpm) and hydrodynamic conditions (375 rpm).

[59, 62]. The particular morphologies of nanoplatelets were a consequence of the interaction between soluble tungsten species and fluoride anions during the precipitation process [59], being hydrodynamic conditions especially important [23].

Under static conditions (0 rpm), current densities recorded during the whole anodization process were notably lower than under hydrodynamic conditions. Moreover, steady-state values were attained much earlier than with rotation, indicating that the WO_3 nanoplatelet layer completely covered the electrode surface after ~2000 s from the beginning of the anodization process. These facts imply that the electrode rotation permitted the ions in the electrolyte (F^- and H^+) to transport to the electrode more rapidly, resulting in higher current densities being measured at the working electrode due to the enhancement of the WO_3 compact layer dissolution. Consequently, an increase in the rotation speed increased the release of soluble species from the electrode surface, which would result in a higher precipitation rate of hydrated WO_3 in the form of nanoplatelets.

Photoelectrochemical characterization of the nanostructures was performed under simulated sunlight illumination AM 1.5 (100 mW cm^{-2}) imposing an external polarization of 1 V (vs Ag/AgCl). Photocurrent density-potential curves for the three different WO_3 nanostructures presented in **Figures 9** and **10** are shown in **Figure 12**. It can be observed that nanoplatelets anodized under static conditions (0 rpm) provided the lowest photocurrent density (~0.41 mA cm^{-2} at 1 V). Nanostructures anodized under hydrodynamic conditions (in the different electrolytes) showed a large enhancement of their photoelectrocatalytic activity (~1.51 mA cm^{-2} at 1 V and ~1.86 mA cm^{-2} at 1 V for nanostructures anodized in the presence of NaF and H_2O_2, respectively). This clear improvement is directly related to the increase of the electrochemically active surface area in nanostructures synthesized under hydrodynamic conditions. As explained earlier, nanoplatelets formed in the presence of NaF and with rotation grew in a tree-like manner forming globular clusters, which made this new nanoplatelet configuration

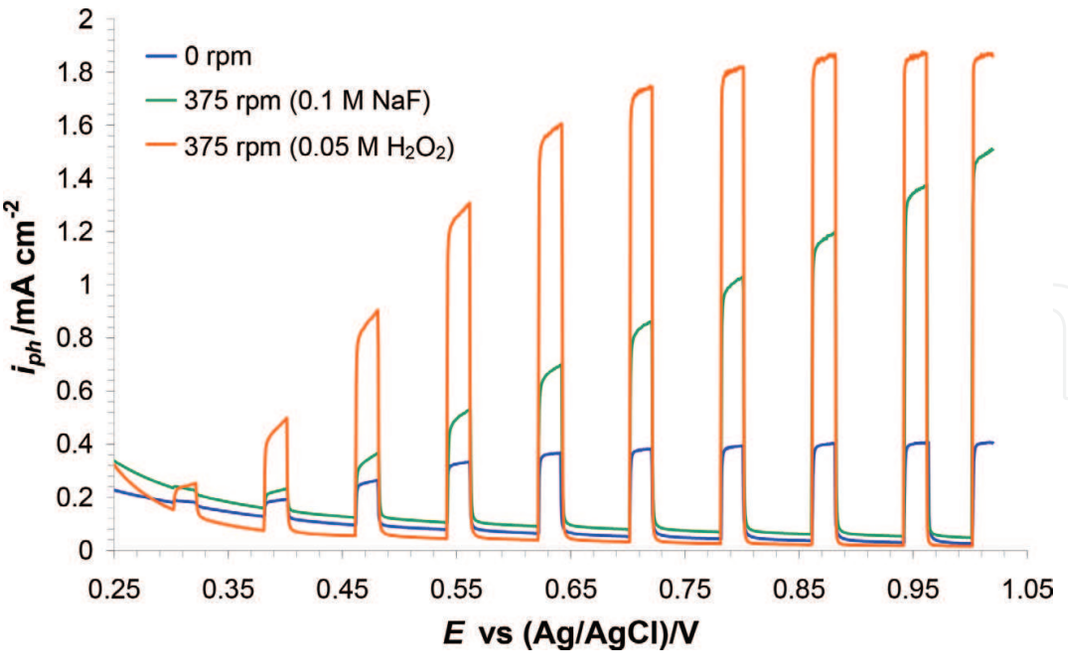

Figure 12. Photocurrent density-potential curves for the three different WO_3 nanostructures presented in **Figures 9** and **10**.

expose much more active area than normal nanoplatelets fabricated at 0 rpm. In the presence of 0.05 M H_2O_2, the obtained nanoplatelets were very small and they aggregated forming very thin layers, also resulting in an increase in the surface area with respect to other WO_3 nanoplatelets and in higher photoelectrochemical efficiencies.

4. Fe_2O_3

Iron oxide nanostructures were made by electrochemical anodization in order to evaluate the effect of hydrodynamic conditions on the formed nanostructures. Prior to anodization, iron rods were abraded with SiC papers of 220, 500 and 4000, sonicated in ethanol, rinsed with distilled water and dried in nitrogen stream. Electrochemical anodization was carried out at room temperature with an ethylene glycol-based solution with 0.1 M NH_4F and 3% vol. H_2O for 15 min at 50 V with iron rod as working electrode and a platinum foil as counter electrode [63]. Different rotation speeds: 0, 1000, 2000 and 3000 rpm, corresponding to Reynolds numbers of 0, 165, 325 and 490, respectively, were applied. Once synthesized, samples were annealed in argon atmosphere for 1 h at 500°C at a heating rate of 15°C · min^{-1}, and cooled within the furnace by natural convection [21].

4.1. Electrochemical anodization

Figure 13 shows the different obtained curves during anodization where three stages can be seen for all the cases (scheme in **Figure 13**). In the first stage, an abrupt drop in the current density from 80 mA · cm^{-2} to less than 15 mA·cm^{-2} (in the case of 0 rpm) and less than 25 mA · cm^{-2} (in the case of hydrodynamic conditions), indicated a formation of an insulating compact oxide layer (Fe_2O_3) on the iron substrate according to Eq. (3).

http://dx.doi.org/10.5772/intechopen.78303

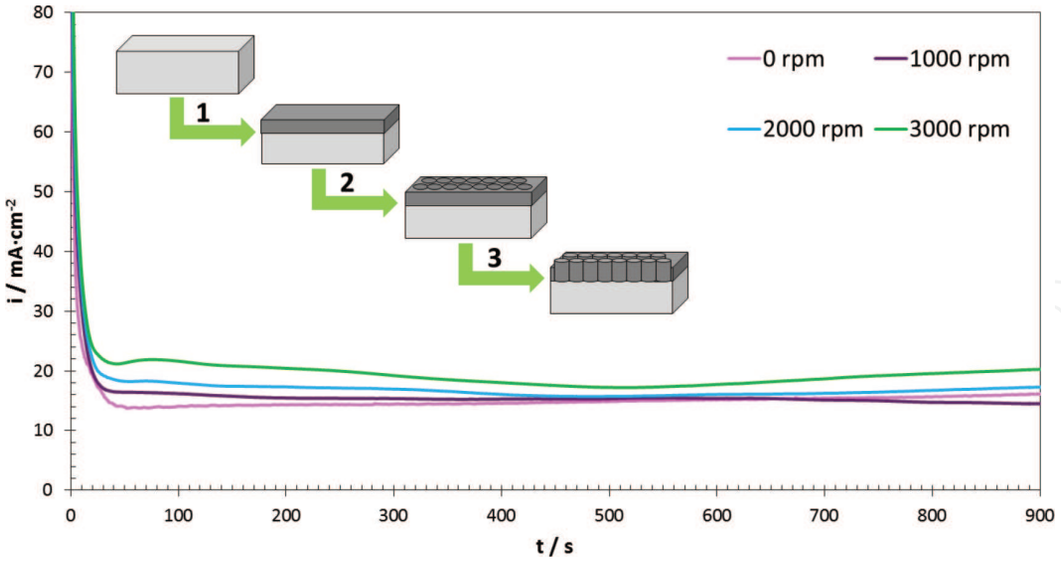

Figure 13. Current density vs. time curves during electrochemical anodization of iron under different electrode rotation speeds. Inset shows a scheme of the process occurring in the electrode during anodization.

In the second stage, a slight increase in current density indicated that tiny pits occur in the surface of the compact layer, followed by the formation of the nanostructures resulting in a decrease in resistance. This process occurs because of the fluoride ions (F^-) and the applied potential which lead to partial dissolution of the compact layer forming the nanoporous structure as Eq. (4) indicates.

$$2Fe + 3H_2O \rightarrow Fe_2O_3 + 3H_2 \tag{3}$$

$$Fe_2O_3 + 12F^- + 6H^+ \rightarrow 2[FeF_6]^{3-} + 3H_2O \tag{4}$$

Finally, in the third stage, further dissolution and cation-cation repulsion occurs and the nanoporous structure leads to a nanotubular one. This occurs until equilibrium between the formation of the oxide layer and its chemical dissolution by F^- is reached. In this way, current density remains almost constant and the formation of nanotubular structure stops [64, 65].

According to **Figure 13**, the formation of the nanostructure under stagnant conditions (0 rpm) leads to lower values of the current density in comparison to the ones synthesized under hydrodynamic conditions. In fact, the higher the rotation speed the higher the current density, achieving the maximum value for the samples anodized at 3000 rpm. This is because steady-state current density is controlled by diffusion processes, hence stirring the iron rods during anodization increases the diffusion and then, current density increases [66, 67].

4.2. Structural characterization

A field emission scanning electron microscope was used in order to evaluate the morphology of the synthesized nanostructures. Moreover, crystalline structure of the samples was evaluated by a confocal Raman microscope with the aim to determine crystalline phases present in the nanostructures.

Figure 14a shows the morphology obtained for the samples under stagnant conditions. In this case, a cracked porous initiation layer appears over the nanotubes, partially covering the entrances of the tubes. This initiation layer results in a decrease in the efficiency of the nanostructures since they might be less accessible to light. On the contrary, **Figure 14b** shows that the initiation layer is etched and the nanotubes are accessible to light irradiation, which leads to higher photoactivity. Nanotubular morphology is advantageous for photoelectrochemical water splitting since it improves electron transport behavior with the tubular orientation. Furthermore, nanotubes avoid short hole diffusion lengths problem since tubes walls make shorter the route from the places where the holes are generated to the surfaces where oxidation reactions are occurring [68].

Figure 14c illustrates the morphology of the samples synthesized at 2000 rpm, and at this rotation speed, the nanotubes collapse and seem to be stacked, so the nanotubes are unseen

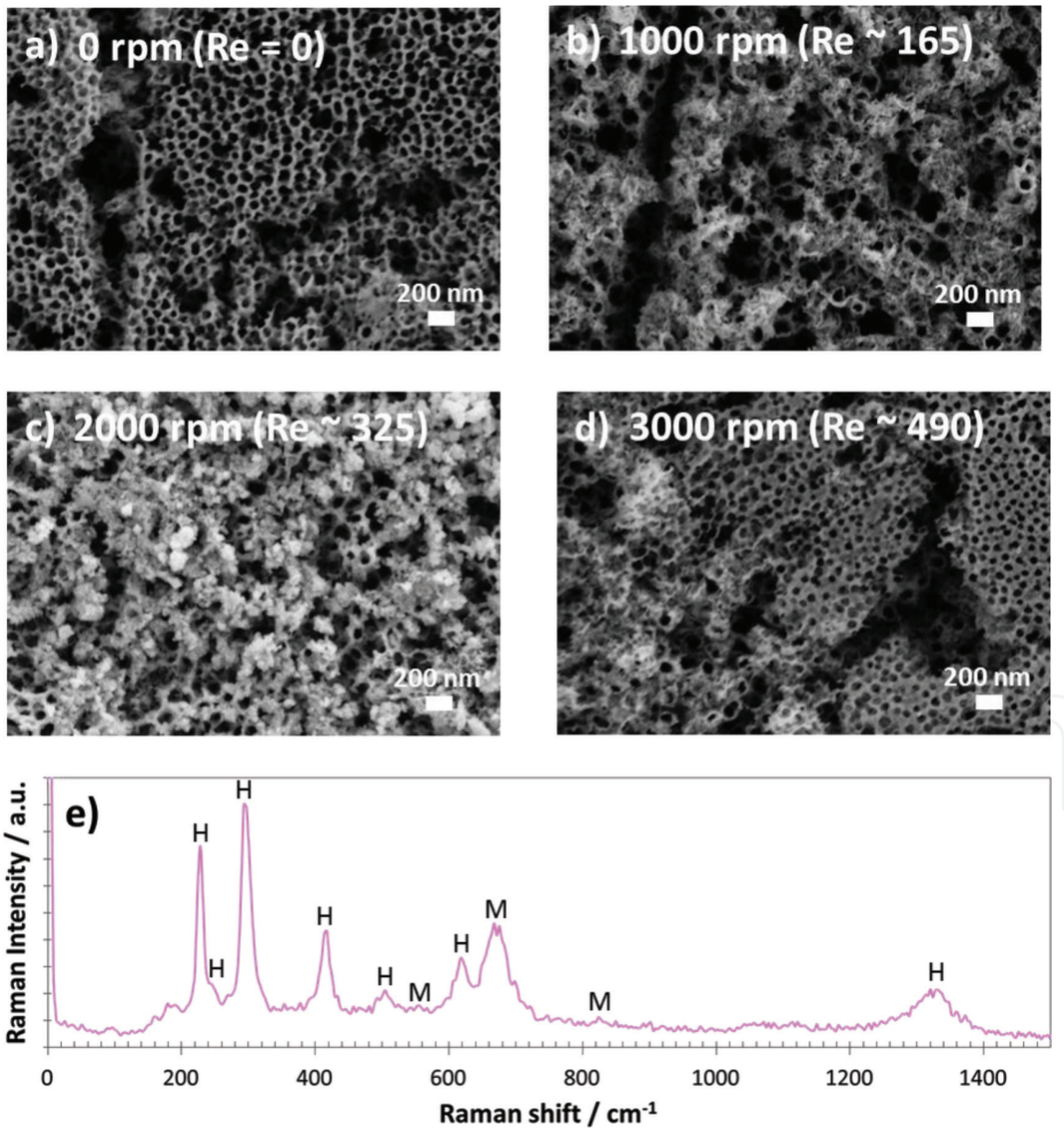

Figure 14. FE-SEM images of the nanostructures synthesized under different electrode rotation speeds: (a) 0 rpm, (b) 1000 rpm, (c) 2000 rpm and (d) 3000 rpm, and (e) Raman spectrum of the nanostructures.

and the top morphology seems to be chaotic. This morphology results in less photoactivity since light irradiation cannot go deep into the nanotubes. On the other hand, when rotation speed is 3000 rpm (see **Figure 14d**), the morphology is a mixture between what occurs at 0 and 2000 rpm, that is, the nanotubes are collapsed and stacked and an initiation layer appears in some parts of the nanostructure covering the tubes [69]. Hence, illumination is not effective in this case, and the photoactivity is affected. This could be due to the fact that at 3000 rpm, some vortex could be formed and then the conditions are non-homogeneous during anodization.

On the other hand, thickness of the nanostructures were measured, and they were comprised between 810 and 870 nm in all cases, which indicated that rotation speed does not affect the thickness of the synthesized nanostructures [69].

Raman spectroscopy was measured with a neon laser 632 nm with ~700 μW. Raman spectra of all the samples were the same, suggesting that rotation speed does not change the crystalline structure of the formed nanostructures. **Figure 14e** shows a Raman spectrum as an example. The Raman shift at which appear the peaks indicates that the nanostructures are mainly composed of hematite with peaks at roughly 229 cm^{-1} (A_{1g}), 249 cm^{-1} (E_g), 295 cm^{-1} (E_g), 414 cm^{-1} (E_g), 500 cm^{-1} (A_{1g}), 615 cm^{-1} (E_g) and 1317 cm^{-1} (2nd order). However, some peaks appearing at approximately 554 cm^{-1}, 672 cm^{-1} and 820 cm^{-1} also indicated the presence of some amount of magnetite [70, 71].

4.3. Photoelectrochemical water splitting tests

For the photocurrent density versus potential measurements the potential was varied from −0.4 to +0.6 $V_{Ag/AgCl}$ at a scan rate of 2 mVs^{-1}.

Figure 15 shows that the highest photocurrent density values were achieved for the nanostructure synthesized at 1000 rpm (reaching 0.130 mA · cm^{-2} at 0.54 $V_{Ag/AgCl}$), which indicated its suitability as photocatalyst for water splitting [69]. This is in agreement with FE-SEM images

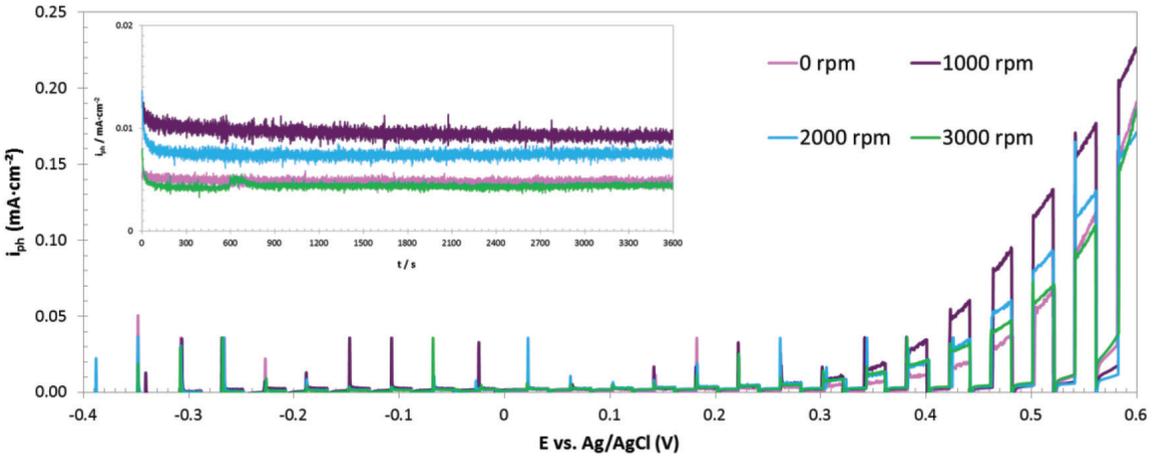

Figure 15. Water splitting tests in 1 M KOH of the nanostructures synthesized at the different electrode rotation speeds. Inset shows stability tests of the synthesized nanostructures under illumination at 0.35 $V_{Ag/AgCl}$ for 1 h in 1 M KOH. Simulated AM 1.5 (100 mW · cm^{-2}) illumination was used for the light conditions.

since they revealed that the morphology of the nanostructures synthesized at 1000 rpm was the most adequate for being illuminated in photoelectrochemical measurements.

Furthermore, inset of **Figure 15** indicates that all synthesized nanostructures were stable against photocorrosion at the indicated conditions.

4.4. Mott-Schottky analysis

For the Mott-Schottky analysis, the potential was swept from the OCP value (~ −0.3 V) in the negative direction at 28 mV s^{-1} with an amplitude signal of 0.01 V at a frequency value of 5 kHz.

Figure 16 shows MS plots for all the synthesized nanostructures under dark (A) and light (B) conditions, indicating a positive slope corresponding to an n-type semiconductor. Note that the higher the slopes of the linear region in MS plots, the lower the electron donor density according to Mott-Schottky equation used for an n-type semiconductor (Eq. (2)), with an assumed ε_r of 80 for the nanostructures [72, 73].

Table 3 shows the results for the different nanostructures and all the values are in the order of 10^{19} cm^{-3}, regardless the rotation speed during anodization. However, the samples anodized at 0 and 3000 rpm achieved donor density values too high which is detrimental for the

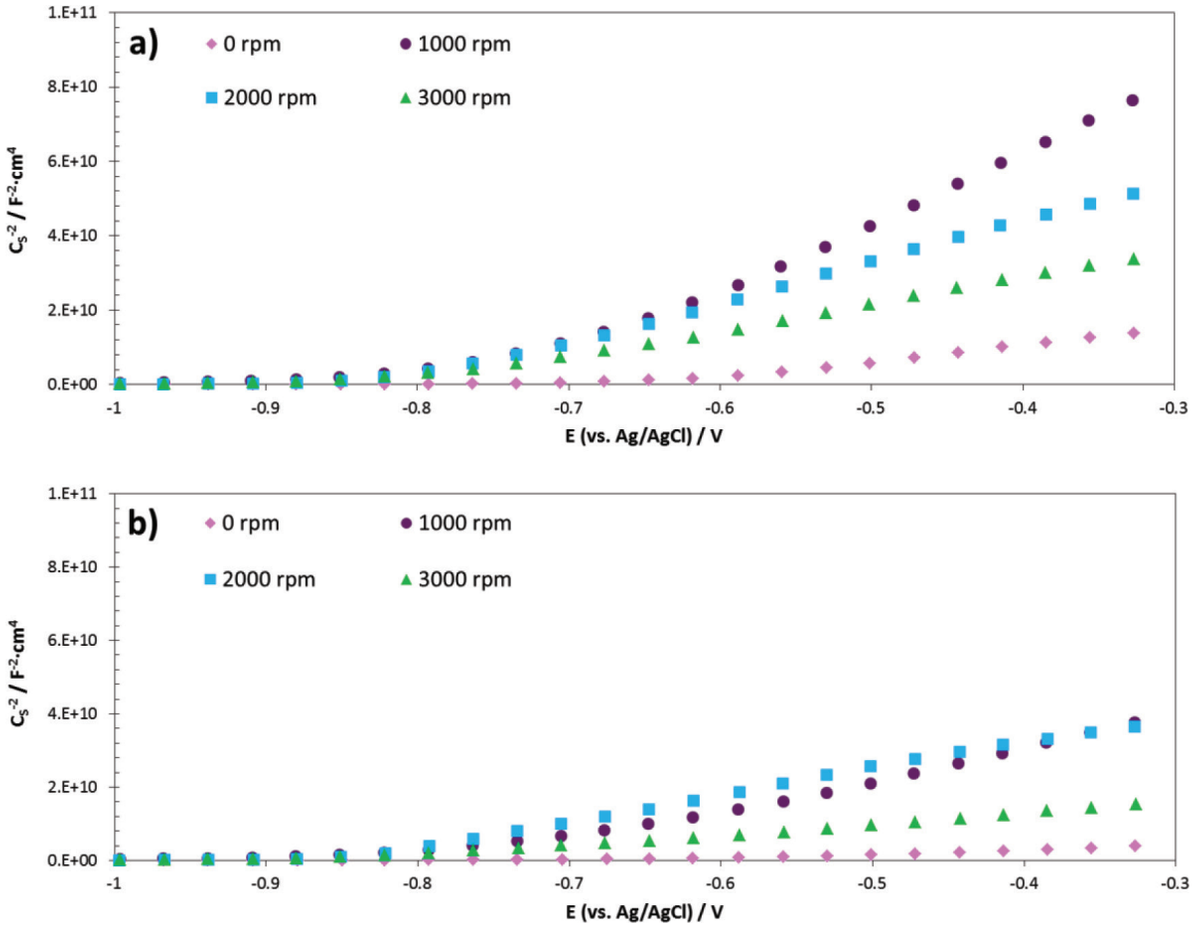

Figure 16. MS analysis of the nanostructures synthesized at the different electrode rotation speeds under dark (a) and 1.5 AM (100 mW · cm^{-2}) illumination (b) conditions in 1 M KOH.

http://dx.doi.org/10.5772/intechopen.78303

Rotation speed/rpm	Conditions	N_D (10^{19})/cm^{-3}	$E_{FB}/V_{Ag/AgCl}$
0 rpm	Dark	4.0 ± 1.0	−0.64 ± 0.05
	Light	14.3 ± 3.5	−0.63 ± 0.05
1000 rpm	Dark	1.0 ± 0.2	−0.76 ± 0.04
	Light	2.2 ± 0.7	−0.78 ± 0.03
2000 rpm	Dark	1.6 ± 0.6	−0.80 ± 0.08
	Light	2.4 ± 0.3	−0.85 ± 0.09
3000 rpm	Dark	2.5 ± 1.0	−0.80 ± 0.03
	Light	5.8 ± 0.7	−0.82 ± 0.03

Table 3. Values of donor density (N_D) and flat band potential (E_{FB}) for the samples synthesized at the different electrode rotation speeds.

photoelectrochemical water splitting since the defects could act as carrier traps (trapping the electrons or holes) [42]. Hence, the efficiency of the water splitting is lower as shown in **Figure 16**. On the contrast, lower donor density values, as in the case of the nanostructure synthesized at 1000 rpm, achieved better photoelectrochemical results (see **Figure 16**) since it avoids recombination processes. This indicates that donor density is a parameter that considerably affects the efficiency of the water splitting.

On the other hand, flat band potential (E_{FB}) is related to the potential drop at the depletion space charge layer ($\Delta\phi_{SC}$) and to the applied external potential (E) according to Eq. (5). Then, the higher and more negative flat band potential, the lower recombination rate [6].

$$\Delta\phi_{SC} = E - E_{FB} \tag{5}$$

Table 3 shows that the flat band potential does not vary for the different nanostructures, which in fact demonstrates that electrode rotation speed during anodization does not affect flat band potential of the synthesized nanostructures.

5. ZnO/ZnS heterostructures

The influence of hydrodynamic conditions was studied for ZnO/ZnS heterostructures obtained from anodization of zinc (0.5 cm^2 area exposed to the electrolyte) in glycerol/water (60:40 vol%) media with 0.025 M NH_4F and 0.2 M Na_2S. Nanostructures were synthesized at different voltages: 20, 30 and 40 V. The advantage of this type of heterostructure is the good photocatalytic behavior of ZnS, which in combination with ZnO could reduce the recombination rate of the charge carriers due to their separated band gaps.

5.1. Morphological characterization

As an example of the nanostructures of ZnO/ZnS obtained from anodization of zinc, **Figure 17** shows the FESEM images of top and cross-sectional views of the samples anodized at different voltages and hydrodynamic conditions. It has been demonstrated [22, 74] that anodization

of zinc in aqueous electrolytes containing both sulfide and fluoride generates a top compact layer and an underneath nanostructure. The former mainly consists of ZnS and the latter of ZnO. That is, the ZnO/ZnS heterostructures grow under the compact ZnS layer. In this way, **Figure 17a** zinc shows the top surface of the nanostructure obtained at 20 V and under static conditions, there, it can be clearly observed the rough ZnS top layer surface. Under stagnant conditions (0 rpm) the anodization of zinc is not homogeneous, since bubbles are formed at the anode surface, and consequently, the formation of precipitates takes place. On the other hand, **Figure 17b** and **c** shows that, when anodization is performed stirring the zinc road (under hydrodynamic conditions), a smooth ZnS top layer is formed. If we compare the heterostructures synthetized at 1000 and at 3000 rpm (**Figure 17b** and **c**, both at 20 V), there is a change in the morphology of the ZnO/ZnS samples from a porous sponge type (**Figure 17b**)

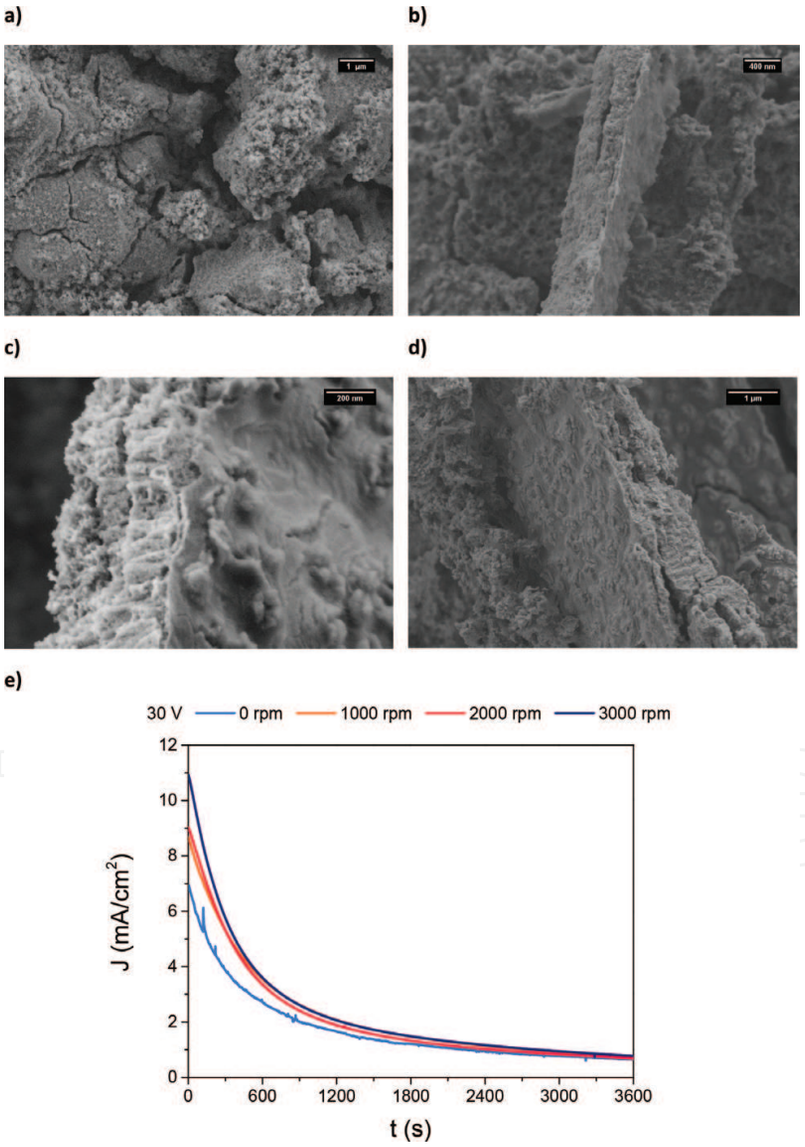

Figure 17. FE-SEM images of the ZnO/ZnS nanostructures anodized at 20 V under static conditions (a), at 1000 rpm (b) and 3000 rpm (c) and at 40 V and under static conditions (d). Current densities recorded during anodization for all the samples anodized at 30 V and at the different rotation speeds (e).

to a porous tubular morphology (**Figure 17c**). Therefore, as rotation speed is increased during anodization, the nanotubular morphology is predominant. This change in morphology continues as anodization potential is increased. In fact, as it can be appreciated in **Figure 17d**, a porous tubular morphology is obtained when anodization is carried out for higher anodization potentials (40 V) even under stagnant conditions. This might be explained taking into consideration that at higher anodization potentials, nanostructures grow faster [75, 76], which involves a lower oxide dissolution, and consequently, a tubular morphology. Besides, the length of the nanostructures was measured obtaining the following values: ~360–600 nm at 20 V, ~800–1100 nm at 30 V and ~1100–1400 nm at 40 V. Thus, longer nanostructures are formed at higher anodization voltages, regardless the hydrodynamic conditions. In this case, longer nanostructures possess a high surface/volume relation, increasing the interaction with light and the electrolyte, and consequently, improving their photocatalytic activity.

5.2. Anodization profile: current densities vs. time

Figure 17e shows, as an example, the current density profiles during the anodization process at 30 V and at the different studied hydrodynamic conditions (0, 1000, 2000 and 3000 rpm). For all cases, the tendency of the current densities is to sharply decrease at the beginning of the anodization, owing to the ZnS precursor layer formation. After that decrease, the current densities continue decreasing until, finally, they stabilize. This tendency is typical of an oxide layer formation in glycerol-based electrolytes [22]. Additionally, it is important to highlight that the higher current density values obtained for the samples anodized stirring the zinc rod are in agreement with the enhancement of the diffusion of the fluoride ions due to the flowing conditions [77]. Besides, the background noise obtained in the current density register of the heterostructure synthesized under static conditions is related to the formation of oxygen bubbles in the zinc surface of the rod during anodization, which generates an irregular anodization of the surface.

It is important to point out that the profiles of current densities versus time for the rest of the heterostructures anodized at 20 and 40 V follow the same trend with hydrodynamic conditions. However, the current densities possess higher values when samples are anodized at higher potentials.

5.3. Crystalline structure characterization

Figure 18a shows, as an example, the Raman spectra of the annealed ZnO/ZnS heterostructures anodized at 30 V at the different hydrodynamic conditions (0, 1000, 2000 and 3000 rpm). Zinc is characterized by a strong broad background signal, which hinders the Raman peaks (**Figure 18a**). This response is associated with the photoluminescence (PL) due to a broad defect band emission in the nanostructures, such as oxygen vacancies [22, 78]. This high concentration of defects was produced due to the absence of oxygen in the atmosphere during the thermal treatment (samples were annealed for 3 h at 375°C in an argon atmosphere), so the evaporated oxygen present in the material cannot be replaced [79] and therefore, the density of oxygen vacancies increases. Then, X-Ray Diffraction (XRD) tests were carried out in order to check the crystalline structure of the annealed samples. **Figure 18b** shows, as an example, the XRD spectrum for the ZnO/ZnS heterostructure anodized at 30 V and at 2000 rpm.

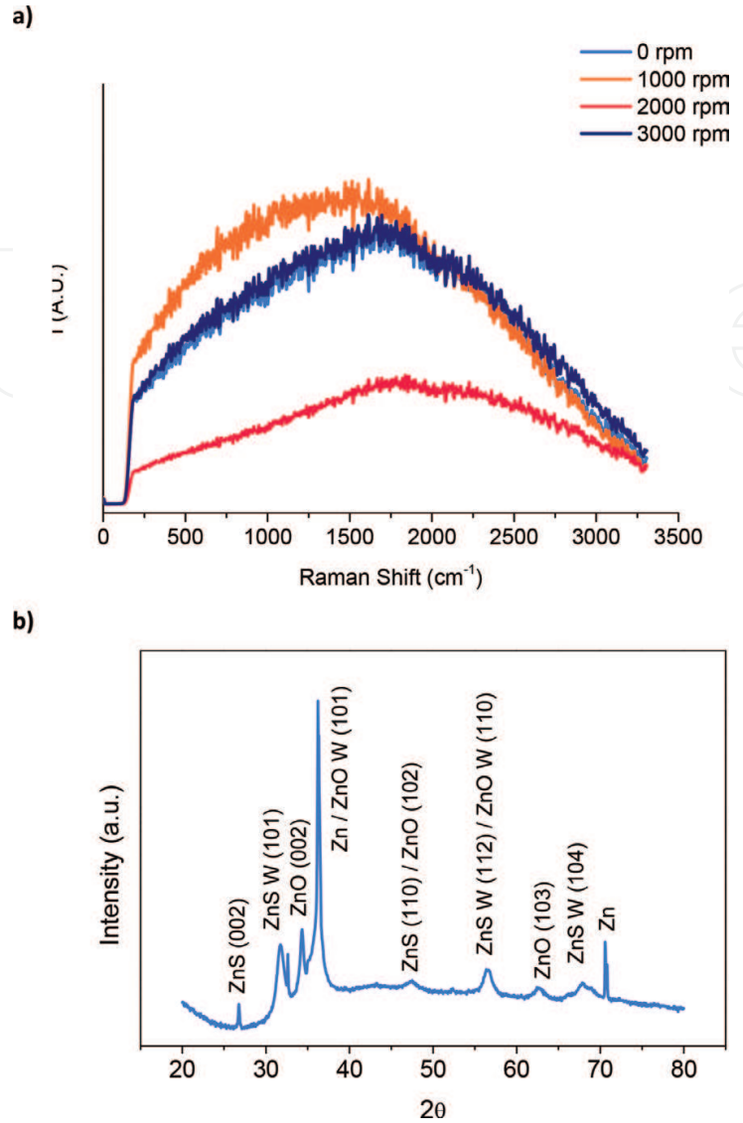

Figure 18. Raman spectra of the ZnO/ZnS heterostructures annealed at 375°C in argon atmosphere for 4 h anodized at 30 V and at 0, 1000, 2000 and 3000 rpm (a) and XRD spectra of the ZnO/ZnS heterostructure anodized at 30 V and 2000 rpm after the annealing treatment.

In the XRD spectra shown in **Figure 18b**, the presence of both ZnO and ZnS can be clearly demonstrated due to the presence of their characteristic peaks [74]. The peak at 25° is related to the ZnS phase with the orientation of (002) [74]. The peaks situated at 36° and 70° are associated with the refraction produced by the polycrystalline Zn substrate [74]. The high intensity of the peak centered at 36° is characteristic of the wurtzite ZnO phase, with an orientation of (101) [80], which is the most abundant phase of the heterostructures. Another ZnO characteristic peak is the one roughly centered at 34°, which corresponds to the orientation (002) [81]. The peaks at 32°, 56° and 67° are associated with the wurtzite ZnS phase with the orientations (101), (112) and (104), respectively [81]. Besides, the peaks centered at 48° and 63° are related, the former, with the ZnS phase with an orientation of (110) and the ZnO phase with an orientation of (102), and the latter, with the ZnO phase with an orientation of (103) [74, 80, 81].

http://dx.doi.org/10.5772/intechopen.78303

5.4. Photoelectrochemical characterization

The ZnO/ZnS nanostructures were characterized as photoanodes in a previously degasified solution of 0.24 M Na_2S and 0.35 M Na_2SO_3 [22]. **Figure 19** shows the photocurrent densities applying different potentials obtained under simulated sunlight AM 1.5 conditions for the different anodization potentials (20, 30 and 40 V) at the studied hydrodynamic conditions (0, 1000, 2000 and 3000 rpm).

In **Figure 19a**, it can be observed that the dark current density values for the ZnO/ZnS heterostructures anodized at 20 V are, in general, high. This fact might be related to a low

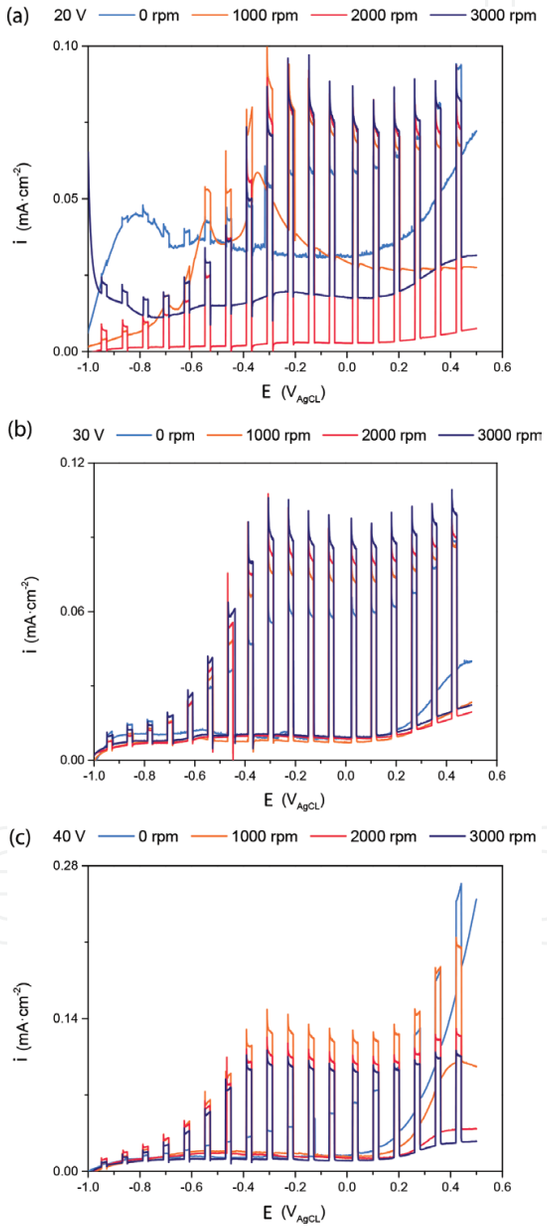

Figure 19. Photocurrent densities vs. applied potential of the ZnO/ZnS heterostructures anodized at 20 V (a), 30 V (b) and 40 V (c) measured in a 0.24 M Na_2S and 0.35 M Na_2SO_3 solution under AM 1.5 illumination.

photocorrosion resistance and could be occasioned by the heterogeneous ZnS precursor layer formed when anodization is performed at 20 V (this was confirmed in FESEM characterization, see **Figure 17a**). On the other hand, when anodization was performed at higher voltages, photocorrosion resistance is increased (**Figure 19b** and **c**), regardless the applied hydrodynamic conditions. In particular, for applied potentials of −0.4 and 0.2 V, the ZnO/ZnS heterostructures show a good stability, since the dark current densities are close to zero and the photocurrent densities are high. Besides, the photocurrent densities for the nanostructures anodized at 30 and 40 V increase for the heterostructures anodized under hydrodynamic conditions. This could be related to the morphology obtained for the nanostructures anodized under hydrodynamic conditions, which showed more nanotubular aspects (**Figure 17**) as the rotation speed was increased, which enhances the charge separation [16, 82–85]. Hence, the photocatalytic response is improved.

Figure 19c shows that the ZnO/ZnS heterostructures anodized at 40 V and under hydrodynamic conditions present the best photocatalytic behavior in terms of higher photocurrent densities and good photocorrosion resistance. In particular, the best conditions were obtained for the ZnO/ZnS heterostructures anodized at 40 V and at 1000 rpm, where the photocurrent density for photoelectrochemical water splitting increased in 100% with respect to the one anodized at 20 V and at 0 rpm, and in a 71% in relation to the photocurrent density obtained for the heterostructure anodized at 20 V and 1000 rpm.

6. Conclusions

In this chapter, the effect of rotating the electrode during electrochemical anodization (hydrodynamic conditions) has been evaluated for different metal oxides. In all cases, hydrodynamic conditions enhanced the photoelectrochemical response of the nanostructures in photoelectrochemical water splitting process.

For nanostructures of TiO_2, hydrodynamic conditions in ethylene glycol media removed the initiation layer over the nanotubes, whereas in glycerol-based electrolytes, rotating the electrode changed the morphology from nanotubes to nanosponges, increasing then the porosity of the structure. For the nanostructures formed in both electrolytes, the surface area increased, resistance values decreased (as EIS showed) and flat band potential became more negative (as MS plots indicated).

In the case of WO_3 nanostructures, the ones synthesized under hydrodynamic conditions presented high active surface area. Furthermore, in the presence of NaF and rotating the electrode, the nanoplatelets grew in a tree-like manner forming globular clusters with more exposed area than in the case of nanostructures synthesized under stagnant conditions. When H_2O_2 is present in the electrolyte, the nanoplatelets were very small, and they aggregated forming very thin layers with high surface areas, which in turn resulted in higher photoelectrochemical efficiencies.

For nanostructures of iron oxide (mainly α-Fe_2O_3), stagnant conditions resulted in nanostructures with an initiation layer that partially covered the top of the nanotubular structure. This

layer was removed under hydrodynamic conditions, in particular at 1000 rpm. At higher rotation velocities, collapsed and stacked nanostructures were formed, which caused lower photoelectrochemical efficiencies. Rotating the electrode during anodization at 1000 rpm led to nanotubular structures with suitable donor densities values and flat band potentials (as MS results indicated), which enhanced photoelectrochemical results.

In the case of ZnO/ZnS heterostructures, high applied potentials and hydrodynamic conditions during anodization led to nanotubular morphology which resulted in higher photoelectrochemical performance. In particular, heterostructures anodized at 40 V and under hydrodynamic conditions presented the best photocatalytic behavior and good photocorrosion resistance.

Acknowledgements

The authors would like to express their gratitude for the financial support to the Ministerio of Economía y Competitividad (Projects CTQ2013-42494-R and CTQ2016-79203-R), for its help in the Laser Raman Microscope acquisition (UPOV08-3E-012) and for the co-finance by the European Social Fund.

Author details

Bianca Lucas-Granados, Rita Sánchez-Tovar, Ramón M. Fernández-Domene and José García-Antón*

*Address all correspondence to: jgarciaa@iqn.upv.es

Department Ingeniería Química y Nuclear, Ingeniería Electroquímica y Corrosión (IEC), Universitat Politècnica de Valencia, Valencia, Spain

References

[1] Garcia Bessegato G, Tasso Guaraldo T, Boldrin Zanoni MV. Enhancement of Photoelectrocatalysis efficiency by using nanostructured electrodes. In: Aliofkhazraei M, editor. Modern Electrochemical Methods in Nano, Surface and Corrosion Science. 1st ed. London: IntechOpen; 2014. pp. 271-319

[2] Daghrir R, Drogui P, Robert D. Photoelectrocatalytic technologies for environmental applications. Journal of Photochemistry and Photobiology A. 2012;**238**:41-52

[3] Garcia-Segura S, Brillas E. Applied photoelectrocatalysis on the degradation of organic pollutants in wastewaters. Journal of Photochemistry and Photobiology C. 2017;**31**:1-35

[4] Eftekhari A, Babu VJ, Ramakrishna S. Photoelectrode nanomaterials for photoelectrochemical water splitting. International Journal of Hydrogen Energy. 2017;**42**:11078-11109

[5] Bak T, Nowotny J, Rekas M, Sorrell CC. Photo-electrochemical hydrogen generation from water using solar energy. Materials-related aspects. International Journal of Hydrogen Energy. 2002;**27**:991-1022

[6] Radecka M, Rekas M, Trenczek-Zajac A, Zakrzewska K. Importance of the band gap energy and flat band potential for application of modified TiO_2 photoanodes in water photolysis. Journal of Power Sources. 2008;**181**:46-55

[7] Lide DR, editor. CRC Handbook of Chemistry and Physics. 89th ed. Boca Raton: CRC Press; 2008

[8] Sánchez-Tovar R, Fernández-Domene RM, García-García DM, García-Antón J. Enhancement of photoelectrochemical activity for water splitting by controlling hydrodynamic conditions on titanium anodization. Journal of Power Sources. 2015;**286**:224-231

[9] Roy P, Berger S, Schmuki P. TiO_2 nanotubes: Synthesis and applications. Angewandte Chemie, International Edition. 2011;**50**:2904-2939

[10] van de Krol R, Principles of photoelectrochemical cells: van de Krol R, Grätzel M, editors. Photoelectrochemical Hydrogen Production, 1st ed. New York: Springer; 2012. p. 13-67

[11] Zhang H, Chen G, Bahnemann DW. Photoelectrocatalytic materials for environmental applications. Journal of Materials Chemistry. 2009;**19**:5089-5121

[12] Zheng H, Ou JZ, Strano MS, Kaner RB, Mitchell A, Kalantar-zadeh K. Nanostructured tungsten oxide - properties, synthesis, and applications. Advanced Functional Materials. 2011;**21**:2175-2196

[13] Bignozzi CA, Caramori S, Cristino V, Argazzi R, Meda L, Tacca A. Nanostructured photoelectrodes based on WO_3: Applications to photooxidation of aqueous electrolytes. Chemical Society Reviews. 2013;**42**:2228-2246

[14] Shinde SS, Bhosale CH, Rajpure KY. Photoelectrochemical properties of highly mobilized Li-doped ZnO thin films. Journal of Photochemistry and Photobiology. B. 2013;**120**:1-9

[15] Quintana M, Edvinsson T, Hagfeldt A, Boschloo G. Comparison of dye-sensitized ZnO and TiO2 solar cells - studies of charge transport and carrier lifetime. Journal of Physical Chemistry C. 2007;**111**:1035-1041

[16] Kushwaha A, Aslam M. ZnS shielded ZnO nanowire photoanodes for efficient water splitting. Electrochimica Acta. 2014;**130**:222-231

[17] Zamiri R, Tobaldi DM, Ahangar HA, Rebelo A, Seabra MP, Belsley MS, Ferreira JMF. Study of far infrared optical properties and, photocatalytic activity of ZnO/ZnS hetero-nanocomposite structure. RSC Advances. 2014;**4**:35383-35389

[18] Mor GK, Varghese OK, Paulose M, Grimes CA. Transparent highly ordered TiO_2 nanotube arrays via anodization of titanium thin films. Advanced Functional Materials. 2005;**15**:1291-1296

[19] Tsuchiya H, Macak JM, Sieber I, Taveira L, Ghicov A, Sirotna K, Schmuki P. Self-organized porous WO_3 formed in NaF electrolytes. Electrochemistry Communications. 2005;**7**:295-298

[20] Mor GK, Varghese OK, Paulose M, Shankar K, Grimes CA. A review on highly ordered, vertically oriented TiO_2 nanotube arrays: Fabrication, material properties, and solar energy applications. Solar Energy Materials & Solar Cells. 2006;**90**:2011-2075

[21] Lucas-Granados B, Sánchez-Tovar R, Fernández-Domene RM, García-Antón J. Study of the annealing conditions and photoelectrochemical characterization of a new iron oxide bi-layered nanostructure for water splitting. Solar Energy Materials & Solar Cells. 2016;**153**:68-77

[22] Sanchez-Tovar R, Fernandez-Domene RM, Montañés MT, Sanz-Marco A, Garcia-Anton J. ZnO/ZnS heterostructures for hydrogen production by photoelectrochemical water splitting. RSC Advances. 2016;**6**:30425-30435

[23] Fernández-Domene RM, Sánchez-Tovar R, Lucas-Granados B, García-Antón J. Improvement in photocatalytic activity of stable WO_3 nanoplatelet globular clusters arranged in a tree-like fashion: Influence of rotation velocity during anodization. Applied Catalysis B: Environmental. 2016;**189**:266-282

[24] Shankar K, Mor GK, Prakasam HE, Yoriya S, Paulose M, Varghese O, Grimes CA. Highly-ordered TiO_2 nanotube arrays up to 220 mm in length: Use in water photoelectrolysis and dye-sensitized solar cells. Nanotechnology. 2007;**18**:065707 (11pp)

[25] Bak T, Nowotny J, Rekas M, Sorrell CC. Photo-electrochemical properties of the TiO_2-Pt system in aqueous solutions. International Journal of Hydrogen Energy. 2002;**27**:19-26

[26] Yahia SAA, Hamadou L, Kadri A, Benbrahim N, Sutter EMM. Effect of anodizing potential on the formation and EIS characteristics of TiO_2 nanotube arrays. Journal of the Electrochemical Society. 2012;**159**:K83-K92

[27] Sánchez-Tovar R, Lee K, García-Antón J, Schmuki P. Formation of anodic TiO_2 nanotube or nanosponge morphology determined by the electrolyte hydrodynamic conditions. Electrochemistry Communications. 2013;**26**:1-4

[28] Costa LL, Prado AGS. TiO_2 nanotubes as recyclable catalyst for efficient photocatalytic degradation of indigo carmine dye. Journal of Photochemistry and Photobiology A: Chemistry. 2009;**201**:45-49

[29] Hsiao PT, Wang KP, Cheng CW, Teng HS. Nanocrystalline anatase TiO_2 derived from a titanate-directed route for dye-sensitized solar cells. Journal of Photochemistry and Photobiology A. 2007;**188**:19-24

[30] Qian L, Du ZL, Yang SY, Jin ZS. Raman-study of titania nanotube by soft chemical-process. Journal of Molecular Structure. 2005;**749**:103-107

[31] Hirschorn B, Orazem ME, Tribollet B, Vivier V, Frateur I, Musiani M. Determination of effective capacitance and film thickness from constant-phase-element parameters. Electrochimica Acta. 2010;**55**:6218-6227

[32] Palmas S, Polcaro AM, Ruiz JR, Da Pozzo A, Mascia M, Vacca A. TiO_2 photoanodes for electrically enhanced water splitting. International Journal of Hydrogen Energy. 2010;**35**:6561-6570

[33] Aïnouche L, Hamadou L, Kadri A, Benbrahim N, Bradai D. Interfacial barrier layer properties of three generations of TiO_2 nanotube arrays. Electrochimica Acta. 2014;**133**:597-609

[34] Jiang Z, Dai X, Middleton H. Investigation on passivity of titanium under steady-state conditions in acidic solutions. Materials Chemistry and Physics. 2011;**126**:859-865

[35] Kong DS, Lu WH, Feng YY, Yu ZY, Wu JX, Fan WJ, Liu HY. Studying on the point-defect-conductive property of the semiconducting anodic oxide films on titanium. Journal of the Electrochemical Society. 2009;**156**:C39-C44

[36] Sazou D, Saltidou K, Pagitsas M. Understanding the effect of bromides on the stability of titanium oxide films based on a point defect model. Electrochimica Acta. 2012;**76**:48-61

[37] Roh B, Macdonald DD. Effect of oxygen vacancies in anodic titanium oxide films on the kinetics of the oxygen electrode reaction. Russian Journal of Electrochemistry. 2007; **43**:125-135

[38] Peng H. First-principles study of native defects in rutile TiO_2. Physics Letters A. 2008;**372**:1527-1530

[39] Tsui LK, Homma T, Zangari G. Photocurrent conversion in anodized TiO_2 nanotube arrays: Effect of the water content in anodizing solutions. Journal of Physical Chemistry C. 2013;**117**:6979-6989

[40] Radecka M, Wierzbicka M, Komornicki S, Rekas M. Influence of Cr on photoelectrochemical properties of TiO_2 thin films. Physica B: Condensed Matter. 2004;**348**:160-168

[41] Carp O, Huisman CL, Reller A. Photoinduced reactivity of titanium dioxide. Progress in Solid State Chemistry. 2004;**32**:33-177

[42] Wang D, Zhang X, Sun P, Lu S, Wang L, Wang C, Liu Y. Photoelectrochemical water splitting with rutile TiO_2 nanowires array: Synergistic effect of hydrogen treatment and surface modification with anatase nanoparticles. Electrochimica Acta. 2014;**130**:290-295

[43] Morgan BJ, Watson GW. Polaronic trapping of electrons and holes by native defects in anatase TiO_2. Physical Review B. 2009;**80**:233102

[44] Irie H, Watanabe Y, Hashimoto K. Nitrogen-concentration dependence on photocatalytic activity of $TiO_{2-x}N_x$ powders. The Journal of Physical Chemistry. B. 2003;**107**:5483-5486

[45] de Tacconi NR, Chenthamarakshan CR, Yogeeswaran G, Watcharenwong A, de Zoysa RS, Basit NA, Rajeshwar K. Nanoporous TiO_2 and WO_3 films by anodization of titanium and tungsten substrates: Influence of process variables on morphology and photoelectrochemical response. The Journal of Physical Chemistry. B. 2006;**110**:25347-25355

[46] Nah YC, Ghicov A, Kim D, Schmuki P. Enhanced electrochromic properties of self-organized nanoporous WO_3. Electrochemistry Communications. 2008;**10**:1777-1780

[47] Lai CW, Sreekantan S. Fabrication of WO_3 nanostructures by anodization method for visible-light driven water splitting and photodegradation of methyl orange. Materials Science in Semiconductor Processing. 2013;**16**:303-310

[48] Ou JZ, Balendhran S, Field MR, McCulloch DG, Zoolfakar AS, Rani RA, Zhuiykov S, O'Mullane AP, Kalantar-zadeh K. The anodized crystalline WO_3 nanoporous network with enhanced electrochromic properties. Nanoscale. 2012;**4**:5980-5988

[49] Ou JZ, Rani RA, Balendhran S, Zoolfakar AS, Field MR, Zhuiykov S, O'Mullane AP, Kalantar-zadeh K. Anodic formation of a thick three-dimensional nanoporous WO_3 film and its photocatalytic property. Electrochemistry Communications. 2013;**27**:128-132

[50] Reyes-Gil KR, Wiggenhorn C, Brunschwig BS, Lewis NS. Comparison between the quantum yields of compact and porous WO_3 photoanodes. Journal of Physical Chemistry C. 2013;**117**:14947-14957

[51] Liu Y, Li Y, Li W, Han S, Liu C. Photoelectrochemical properties and photocatalytic activity of nitrogen-doped nanoporous WO_3 photoelectrodes under visible light. Applied Surface Science. 2012;**258**:5038-5045

[52] Nah YC, Paramasivam I, Hahn R, Shrestha NK, Schmuki P. Nitrogen doping of nanoporous WO_3 layers by NH_3 treatment for increased visible light photoresponse. Nanotechnology. 2010;**21**:105704 (5pp)

[53] Sadek AZ, Zheng H, Breedon M, Bansal V, Bhargava SK, Latham K, Zhu J, Yu L, Hu Z, Spizzirri PG, Wlodarski W, Kalantar-zadeh K. High-temperature anodized WO_3 nanoplatelet films for photosensitive devices. Langmuir. 2009;**25**:9545-9551

[54] Kalantar-zadeh K, Sadek AZ, Zheng H, Bansal V, Bhargava SK, Wlodarski W, Zhu J, Yu L, Hu Z. Nanostructured WO_3 films using high temperature anodization. Sensors and Actuators B: Chemical. 2009;**142**:230-235

[55] Ng C, Ng YH, Iwase A, Amal R. Influence of annealing temperature of WO_3 in Photoelectrochemical conversion and energy storage for water splitting. ACS Applied Materials & Interfaces. 2013;**5**:5269-5275

[56] Cristino V, Caramori S, Argazzi R, Meda L, Marra GL, Bignozzi CA. Efficient photoelectrochemical water splitting by anodically grown WO_3 electrodes. Langmuir. 2011;**27**:7276-7284

[57] Ng C, Ye C, Ng YH, Amal R. Flower-shaped tungsten oxide with inorganic fullerene-like structure: Synthesis and characterization. Crystal Growth & Design. 2010;**10**:3794-3801

[58] Fernández-Domene RM, Sánchez-Tovar R, Segura-Sanchís E, García-Antón J. Novel tree-like WO_3 nanoplatelets with very high surface area synthesized by anodization under controlled hydrodynamic conditions. Chemical Engineering Journal. 2015;**286**:59-67

[59] Fernández-Domene RM, Sánchez-Tovar R, Lucas-Granados B, Roselló-Márquez G, García-Antón J. A simple method to fabricate high-performance nanostructured WO_3 photocatalysts with adjusted morphology in the presence of complexing agents. Materials and Design. 2017;**116**:160-170

[60] Li W, Li J, Wang X, Luo S, Xiao J, Chen Q. Visible light photoelectrochemical responsiveness of self-organized nanoporous WO_3 films. Electrochimica Acta. 2010;**56**:620-625

[61] Wang CK, Lin CK, Wu CL, Wang SC, Huang JL. Synthesis and characterization of electrochromic plate-like tungsten oxide films by acidic treatment of electrochemical anodized tungsten. Electrochimica Acta. 2013;**112**:24-31

[62] Lassner E, Schubert WD. Tungsten. Properties, Chemistry, Technology of the Element, Alloys, and Chemical Compounds. 1st ed. New York: Kluwer Academic/Plenum Publishers; 1999

[63] Lucas-Granados B, Sánchez-Tovar R, Fernández-Domene RM, García-Antón J. Influence of electrolyte temperature on the synthesis of iron oxide nanostructures by electrochemical anodization for water splitting. International Journal of Hydrogen Energy. 2018;**43**:7923-7937

[64] Pervez SA, Kim D, Farooq U, Yaqub A, Choi JH, Lee YJ. Crystalline iron oxide nanotube arrays with high aspect ratio as binder free anode for Li-ion batteries. Physica Status Solidi a - Applications and Materials Science. 2014;**211**:1889-1894

[65] Xie K, Guo M, Huang H, Liu Y. Fabrication of iron oxide nanotube arrays by electrochemical anodization. Corrosion Science. 2014;**88**:66-75

[66] Yasuda K, Schmuki P. Control of morphology and composition of self-organized zirconium titanate nanotubes formed in $(NH_4)_2SO_4/NH_4F$ electrolytes. Electrochimica Acta. 2007;**52**:4053-4061

[67] Macak JM, Hildebrand H, Marten-Jahns U, Schmuki P. Mechanistic aspects and growth of large diameter self-organized TiO2 nanotubes. Journal of Electroanalytical Chemistry. 2008;**621**:254-266

[68] Lee CY, Wang L, Kado Y, Killian MS, Schmuki P. Anodic nanotubular/porous hematite photoanode for solar water splitting: Substantial effect of iron substrate purity. ChemSusChem. 2014;**7**:934-940

[69] Lucas-Granados B, Sánchez-Tovar R, Fernández-Domene RM, García-Antón J. Controlled hydrodynamic conditions on the formation of iron oxide nanostructures synthesized by electrochemical anodization: Effect of the electrode rotation speed. Applied Surface Science. 2017;**392**:503-513

[70] a de Faria DL, Lopes FN. Heated goethite and natural hematite: Can Raman spectroscopy be used to differentiate them. Vibrational Spectroscopy. 2007;**45**:117-121

[71] Jubb AM, Allen HC. Vibrational spectroscopic characterization of hematite, maghemite, and magnetite thin films produced by vapor deposition. ACS Applied Materials & Interfaces. 2010;**2**:2804-2812

[72] Rahman G, Joo OS. Photoelectrochemical water splitting at nanostructured α-Fe_2O_3 electrodes. International Journal of Hydrogen Energy. 2012;**37**:13989-13997

[73] Shen S, Zhou J, Dong CL, Hu Y, Tseng EN, Guo P. Surface engineered doping of hematite nanorod arrays for improved photoelectrochemical water splitting. Scientific Reports. 2014;**4**:6627-6636

[74] Shrestha NK, Lee K, Hahn R, Schmuki P. Anodic growth of hierarchically structured nanotubular ZnO architectures on zinc surfaces using a sulfide based electrolyte. Electrochemistry Communications. 2013;**34**:9-13

[75] Zhou X, Truong Nguyen N, Özkan S, Schmuki S. Anodic TiO_2 nanotube layers:Why does self-organized growth occur — A mini review. Electrochemistry Communications. 2014;**46**:157-162

[76] Khudhair D, Bhatti A, Li Y, Amani Hamedani H, Garmestani H, Hodgson P, Nahavandi S. Anodization parameters influencing the morphology and electrical properties of TiO_2 nanotubes for living cell interfacing and investigations. Materials Science and Engineering: C. 2016;**59**:1125-1142

[77] Sánchez-Tovar R, Fernández-Domene RM, Martínez-Sánchez A, Blasco-Tamarit E, García-Antón J. Synergistic effect between hydrodynamic conditions during Ti anodization and acidic treatment on the photoelectric properties of TiO_2 nanotubes. Journal of Catalysis. 2015;**330**:434-441

[78] He S, Zheng M, Yao L, Yuan X, Li M, Mab L, Shen W. Preparation and properties of ZnO nanostructures by electrochemical anodization method. Applied Surface Science. 2010;**256**:2557-2562

[79] Ogata K, Sakurai K, Fujita S, Fujita S, Matsushige K. Effects of thermal annealing of ZnO layers grown by MBE. Journal of Crystal Growth. 2000;**214/215**:312-315

[80] Farooqi MMH, Srivastava RK. Structural, optical and photoconductivity study of ZnO nanoparticles synthesized by annealing of ZnS nanoparticles. Journal of Alloys and Compounds. 2017;**691**:275-286

[81] Patel PC, Ghosh S, Srivastava PC. Structural, magnetic and optical properties of ZnO nanostructures converted from ZnS nanoparticles. Materials Research Bulletin. 2016;**81**:85-89

[82] Chen S, Thind SS, Chen A. Nanostructured materials for water splitting - state of the art and future needs: A mini-review. Electrochemistry Communications. 2016;**63**:10-17

[83] Zhu J, Zäch M. Nanostructured materials for photocatalytic hydrogen production. Current Opinion in Colloid & Interface Science. 2009;**14**:260-269

[84] Kim Y, Park J, Kim S, Park DW, Choi J. Fabrication of hierarchical ZnO nanostructures for dye-sensitized solar cells. Electrochimica Acta. 2012;**78**:417-421

[85] Sreekantan S, Gee LR, Lockman Z. Room temperature anodic deposition and shape control of one-dimensional nanostructured zinc oxide. Journal of Alloys and Compounds. 2009;**476**:513-518

IntechOpen